

東京大学 大学院新領域創成科学研究科
基盤科学研究系
先端エネルギー工学専攻

平成 19 年度
修士論文

High sensitive laser absorption spectroscopy with Cr:LiSAF

-Cr:LiSAF レーザーを用いた高感度レーザー吸収分光法-

2008 年 2 月提出
指導教員 小紫 公也 助教授

66205 落水 秀晃

Contents

1	Introduction	8
1.1	Background	8
1.2	High enthalpy wind tunnels	10
1.3	Plasma diagnostics	13
1.3.1	Intrusive methods	13
1.3.2	Non-Intrusive methods	15
1.4	Objectives	18
2	Laser absorption spectroscopy for diagnosing high enthalpy flow	19
2.1	Principle of Laser Absorption Spectroscopy	19
2.1.1	Laser Absorption	22
2.1.2	Broadning of absorption profile	22
2.1.3	The way of estimating physical parameters of high enthalpy flow	26
2.1.4	Absorption Target	28
2.2	Measurement system	30
2.2.1	External cavity diode laser (ECDL)	31
2.2.2	Isolator	31
2.2.3	Etalon	32
2.2.4	Photo detector	34
2.2.5	Function generator	34
2.2.6	Power meter	34
2.2.7	Argon glow discharge tube	34
2.2.8	Arc heater	37
2.3	Past results	39

3	High sensitivity laser absorption spectroscopy	41
3.1	High sensitivity laser absorption spectroscopy	41
3.1.1	Free propagation of light in the atomosphere	41
3.1.2	Multireflection cells	41
3.1.3	Cavity ring down spectroscopy (CRDS)	42
3.1.4	Cavity enhanced absorpton spectroscopy (CEAS)	43
3.1.5	Intracavity absorption spectroscopy (ICAS)	44
3.2	Principle of intracavity absorption spectroscopy	46
3.2.1	Laser thereshold power and output power	46
3.2.2	Laser oscillation power with placing plasma into a cavity	49
3.3	Past results of intracavity laser absorption spectroscopy	51
4	Characteristics of Cr:LiSAF laser	53
4.1	Selection of a laser medium	53
4.2	Cr:LiSAF	54
4.3	Tuning characteristics of Cr:LiSAF	56
5	Experimental results and Discussion	59
5.1	Characteristics of Cr:LiSAF Laser (25mm cavity)	59
5.1.1	Experimental system	59
5.1.2	Output spectrum	64
5.1.3	Beam pattern	65
5.1.4	Laser output power	66
5.1.5	Selecting laser wavelength	67
5.2	ICAS measurement with Cr:LiSAF laser (150mm cavity)	70
5.2.1	Characteristics of Cr:LiSAF laser (150mm cavity)	70
5.2.2	The magnification of absorbance in ICAS	72
5.2.3	The measurement of absorbance in ICAS	73
6	Conclusion	76

List of Figures

1.1	Trajectory of various reentry vehicles	9
1.2	Stagnation temperature as a function of test time for various wind tunnels	9
1.3	Pressure specific enthalpy envelops for various plasma wind tunnels	12
1.4	Schematic of mass spectrometer	14
1.5	Schematic of Pitot probe	15
2.1	A transition of the electron by absorbing photon	19
2.2	The variation of probe laser intensity	20
2.3	Absorption coefficient	21
2.4	Grotrian diagram of atomic oxygen	29
2.5	Grotrian diagram of atomic argon	29
2.6	Schematic of the optical system for Ar discharge tube	30
2.7	Schematic of the optical system for arc heater	31
2.8	Block diagram of isolator	32
2.9	The principle feature of an etalon	33
2.10	Arc discharge tube	35
2.11	Ar discharge tube on operating	36
2.12	Arc heater made in Tokyo University	38
2.13	Cross section view of the arc heater made in Tokyo University	38
2.14	Absorbance in pure oxygen and nitrogen/oxygen flows of IRS	40
3.1	Schematic diagram of the long white cell optics and the interface to the spectrometer	42
3.2	Schematic for principle of cavity ring down laser absorption spectroscopy	42
3.3	Schematic for principle of intracavity absorption spectroscopy	44
3.4	Schematic for energy level of four level laser	46
3.5	Schematic of intracavity absorption spectroscopy system with ECDL	51

3.6	The results of intracavity absorption spectroscopy with ECDL	52
4.1	Absorption and the emission spectrum of Cr:LiSAF	54
4.2	Energy level of transition metal ion	55
4.3	Schematic of a coupled cavity	57
4.4	The resonance mode of a coupled cavity	57
5.1	Schematic of Cr:LiSAF laser system with a 25mm-cavity	60
5.2	Picture of pump LD laser system	61
5.3	Picture of Cr:LiSAF crystal	62
5.4	The spectrum of Cr:LiSAF laser (25mm cavity)	64
5.5	The spatial distribution of Cr:LiSAF laser beam	65
5.6	The profile of Cr:LiSAF laser beam	65
5.7	The relationship of pump power and Cr:LiSAF laser output power (25mm cavity)	66
5.8	Schematic of the laser system for selecting wavelength	68
5.9	The result of selecting wavelength	69
5.10	The spectrum of Cr:LiSAF laser (150mm cavity)	70
5.11	The relationship of pump power and Cr:LiSAF laser output power (150mm cavity)	71
5.12	The magnification of absorbance	72
5.13	Schematic of the measurement system	73
5.14	Picture of the measurement system	73
5.15	The absorbances in ICAS and LAS	74

List of Tables

1.1	Plasma wind tunnels in Japan	10
1.2	Plasma wind tunnels in the world	11
1.3	Comparison of LAS,ES and LIF	16
1.4	Diagnostic method	17
2.1	Comparison of broadening effects	26
2.2	Transition data	28
2.3	Operating conditions of the arc heater	39
2.4	Previous measurement for various plasma wind tunnels	39
3.1	Intracavity absorption spectroscopy by several laser types	45
4.1	Laser mediums	53
4.2	The examples of tuning Cr:LiSAF laser	56
4.3	The examples of Cr:LiSAF laser with a coupled cavity	58
5.1	Parameters for estimation	72
5.2	The magnification of absorbance	74
5.3	The parameter of absorption lines	75
5.4	Number density of meta-stable argon	75

Acknowledgments

I would like to express my sincerest gratitude to Assistant Professor Kimiya Komurasaki (Department of Advanced Energy, University of Tokyo) for providing his eager instruction, and encouragements to me.

I would like to express my sincerest gratitude to Professor Kimiya Komurasaki (Department of Aeronautics and Astronautics, University of Tokyo) for his perspective advices.

I give my thanks to Dr.Taku Saiki (Institute for Laser Technology) for his technical advise about laser.

I 'm grateful to Dr.Makoto Matsui (Department of Aeronautics and Astronautics, University of Tokyo) for his many advices about my reserch and experment.

I 'm also grateful to Mr.Hiroki Takayangi (Department of Aeronautics and Astronautics, University of Tokyo) who told me how to experiment and gave me the view about my research.

I wish to give my thanks to Mr.Yasuhisa Oda (Department of Advanced Energy, University of Tokyo) for providing me his help and kindness.

Finally, I wish to thank all members in Araakwa-Komurasaki laboratory who propose a comfortable environment.

Chapter 1

Introduction

1.1 Background

The history of space development and use of space of human beings has just passed through 100 years at last, and is almost the same as the history of an airplane. After the first space flight of Major Gagarin of the Soviet Union, the first manned landing the moon's surface by the spaceship Apollo, and the manned transportation by a space shuttle with improvement and progress of rockets and satellites going, the history are going to the construction of International Space Station. Development of the body which can bear the severe environment at the time of atmosphere reentry is one of the subjects which should be overcome for such space development or space activity. For example, Space shuttle which is a typical spacecraft entries the earth at the velocity of 7km/h ($Mach > 20$), and the gas temperature in front of its nose is heated up 7000K. The relationships of the flight altitude and the enthalpy of a space shuttle, Apollo and Single-Stage-To-Orbit, are shown in Fig.1.1[1]. Many missions which entry atmosphere of the earth or other planet are also performed, such as Mars exploration by Mars Pathfinder, and sample return mission by MUSES-C, etc. It is a key for development of Thermal Protection System (TPS) which protects spacecraft from such severe conditions to overcome this subject from the demand of the above missions.

As indicated by Auweter-Kurtz [2], TPS requires such characteristics as 1) low mass, 2) smooth surface to avoid an early flow change from laminar to turbulent, 3) necessary strength to withstand aerodynamic, aeroelastic, chemical and heat loads, 4) low catalysity not to encourage the recombination heating, 5) high emissivity to promote the radiation cooling. For such TPS developments, ground test facilities are necessary to simulate reentry conditions, because actual flight-tests have many problems such as high cost, difficult in reproducibility and restrictions of measurement equipments.

Because, unfortunately, there is no facility to simulate such severe reentry conditions completely, various types of ground test facilities have been developed to simulate specific conditions as shown in Fig.1-2[1]. Although, ballistic range, shock tubes, expansion tubes and shock tunnels (including reflected shock tunnels, gun tunnels, Stalker tubes) can produce high temperature and high total pressure conditions, their run time is restricted to be several ms to μ s. It is too short for TPS tests because TPS surfaces remains cold and may less interact with the hot gas than actual flight conditions. The short run time also complicates measurement techniques. Therefore, plasma wind tunnels that can produce high temperature conditions for more than several ten minutes are most suitable for TPS tests and widely used in the world.

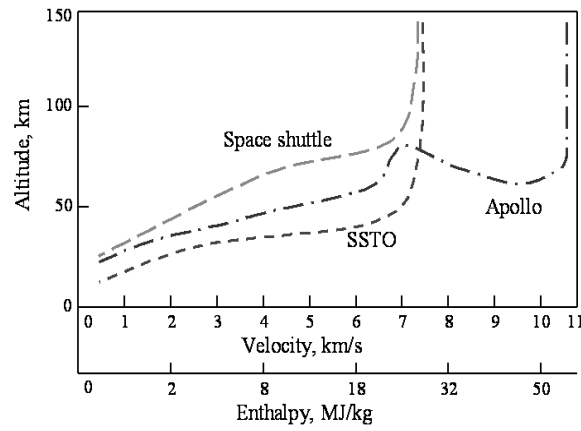


Figure 1.1: Trajectory of various reentry vehicles

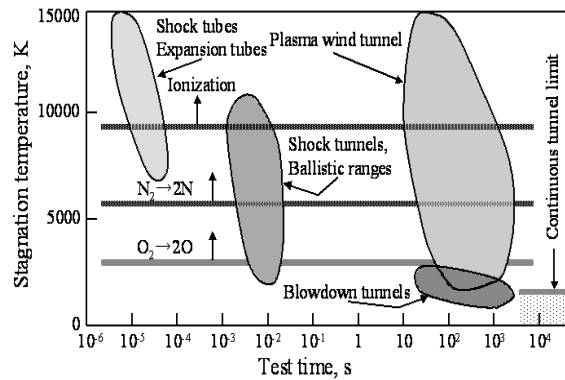


Figure 1.2: Stagnation temperature as a function of test time for various wind tunnels

1.2 High enthalpy wind tunnels

As described in section 1.1, various plasma wind tunnels are developed. Plasma wind tunnels more than 10kW class developed in Japan are shown in Table 1.1[3]. And, plasma wind tunnels developed in the world are shown in Table 1.2

Table 1.1: Plasma wind tunnels in Japan

Affiliation	Type	Input power kW	Total pressure Mpa	Specific enthalpy MJ/kg
ISAS/JAXA	Huels	500	1	16
JUTEM	Constricted	20	0.1	10
Kyusyu Univ.	Constricted	20	0.1	10
Nagoya Univ.	Constricted	12		
ISAS/JAXA	Segmented	1000	1.05	9.5
ISTA/JAXA	Segmented	750		
ISTA/JAXA ^[4]	ICP	110	0.05	25
ISAS/JAXA ^[5]	ICP	10	0.04	32

Table 1.2: Plasma wind tunnels in the world

Country	Facility	Affiliation	Input power MW	Total pressure MPa	Specific enthalpy MJ/kg
Huels					
USA	2.9 in Turbulant Flow	NASA Ames	20	4	9.3
USA	Direct Connect	NASA Ames	50	2.5	9.3
USA	AHSTF	NASA Langley	10	4.5	3.7
USA	H-R	AEDC	40	10	9.3
USA	H-2	AEDC	40	10	9.3
USA	LCAT	Boeing	10	10	14
France	JP200	Aerospatiale	20	6	13.2
France	9MW HP	Aerospatiale	9	13	5.1
France	Simoun	Aerospatiale	5	1.5	14
Germany	L2K	DLR	1	1.4	25.5
Constricted					
Germany	PWK4	Univ.of Stuttgart	0.1	0.1	30
Magnetically stabilized					
Russia	U15-T-1	TsNIIMASH	40	1.2	7.0
Russia	U15-T-2	TsNIIMASH	50	5	8.1
Russia	TT-1	TsNIIMASH	10	8	9.3
Russia	TT-2	TsNIIMASH	6	2.5	46.5
Segmented					
USA	AHF	NASA Ames	20	1	32.5
USA	IHF	NASA Ames	60	1	46.4
USA	TP-1	NASA JSC	10	1	37.1
USA	TP-2	NASA JSC	10	1	37.1
USA	H-1	AEDC	30	12	12
USA	H-3	AEDC	68	12	11
Germany	L3K	DLR	5	1.7	21
Italy	Scirocco	CIRA	70	1.7	45
MPD					
Germany	PWK1	Univ. Stuttgart	0.25	0.1	116
Germany	PWK2	Univ. Stuttgart	1.0	0.05	150
Russia	MPDA-T16	TsNIIMASH	4	0.003	46.5
ICP					
Russia	IPG-3	IPM RASA	0.75	0.03	40
Russia	IPG-4	IPM RASA	0.08	0.1	40
Russia	VTs	TsAGI	1.0	0.08	37.2
Russia	VAT-104	TsAGI	0.24 0.04	37.2	
Russia	U-13-HFP	TsNIIMASH	1.0	0.04	46.5
Germany	PWK3	Univ.of Stuttgart	0.15	0.01	80
France	Comete	Aerospatiale	0.015	0.1	32.6
Belgium	Plasmatron	VKI	1.2	0.1	

Smith classified these plasma wind tunnels into six types which are Huels arc, Constricted arc, Magnetically stabilized, Segmented arc, MagnetoPlasmaDynamic (MPD) and Inductively Coupled Plasma (ICP), according to the heating method. The relationship of stagnation point temperature and specific enthalpy of these six wind tunnels are shown in Fig.1.3 [6].

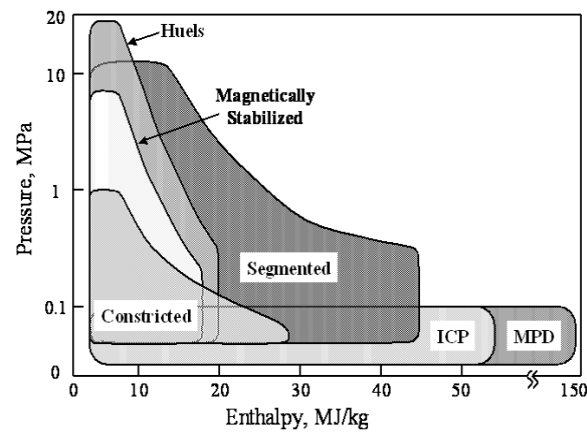


Figure 1.3: Pressure specific enthalpy envelopes for various plasma wind tunnels

1.3 Plasma diagnostics

Although it is necessary to characterize high enthalpy flows for evaluation of TPS performances, their exact conditions such as specific enthalpy, total pressure and number density of species have not been relatively unknown. Therefore, various diagnostics techniques have been developed with the wind tunnels developments [7, 8]. These techniques are classified into intrusive and non-intrusive methods.

1.3.1 Intrusive methods

Intrusive methods are those to put a probe into the flow directly. Although these methods disturb the flow conditions by their insert, they are established methods. In the following paragraph the obtainable parameters and corresponding intrusive methods are described. These are also tabulated and compared with non-intrusive methods in Table 1-3.

Specific enthalpy

The specific enthalpy of the flow is the most important parameter to characterize performances of the wind tunnels and various techniques have been proposed.

Enthalpy balance method This method is very easy and a most widespread one [8]. The specific enthalpy h_{ave} is estimated by the plasma power P_{plasma} or the input power P_{in} and heat loss P_{loss} , expressed as,

$$h_{ave} = \frac{P_{plasma}}{\dot{m}} = \frac{P_{in} - P_{loss}}{\dot{m}}. \quad (1.1)$$

where, \dot{m} is the mass flow rate. In the former case, the plasma power is directly measured by a calorimeter and in the latter case, the heat loss power is estimated by the increase of cooling water temperature [7].

Although this method may give an indicator to characterize the wind tunnels, the estimated specific enthalpy is the averaged over the volume.

Sonic flow method This method developed by Winovich is based on the fact that sonic mass flow is uniquely determined under thermal equilibrium [9]. Then, the choked mass flow is determined by a given specific enthalpy and total pressure. Conversely, the specific enthalpy can be estimated by the mass flow and pressure expressed as,

$$\frac{\dot{m}}{Ap_0} = \frac{\sqrt{2h_0}}{RT_0} \left\{ \frac{\rho^*}{\rho_0} \left(1 - \frac{h^*}{h_0} \right)^{1/2} \right\} \quad (1.2)$$

Here, A is the cross sectional area, h is the enthalpy, p is the pressure, R is the gas constant, T is the temperature, ρ is the density, the subscript 0 refers to stagnation conditions and subscript * refers to conditions at the throat.

In the pressure range $0.025 \text{ MPa} < p_0 < 10 \text{ MPa}$, the above expression considering real gas effects is empirically approximated as [10],

$$\frac{\dot{m}}{Ap_0} = \frac{C}{h_{\text{ave}}^{0.397}} \quad (1.3)$$

Here, C is the constant factor. The effects of boundary layer, non-equilibrium chemistry and heat loss to the nozzle wall were examined. As well as the enthalpy balance method, this method gives only the averaged enthalpy.

Species number density

Mass spectrometer The density and energy distributions of neutral and ionized particles are estimated. A schematic of mass spectrometer is shown in Fig.1.4. The incoming particles are ionized in an ion source and then classified by an energy analyzer. Then, the relative density of each species can be measured. For the absolute measurements, a reference cell is used.

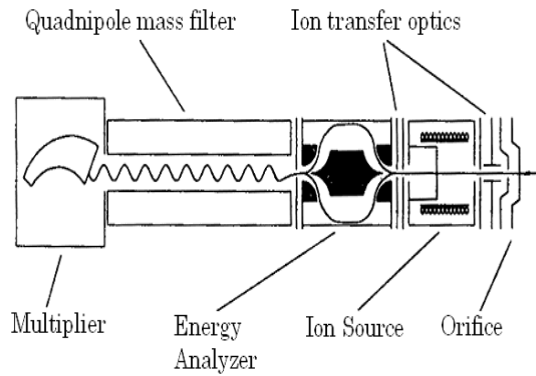


Figure 1.4: Schematic of mass spectrometer

Total pressure

Pitot probe For the total pressure measurement, Pitot probes shown in Fig.1-5 [7] have been widely used. Care should be pair for the difference between subsonic and super sonic flows as described in following paragraph. As for the measurement technique, a hole of the probe should be larger than the mean free path of the gas.

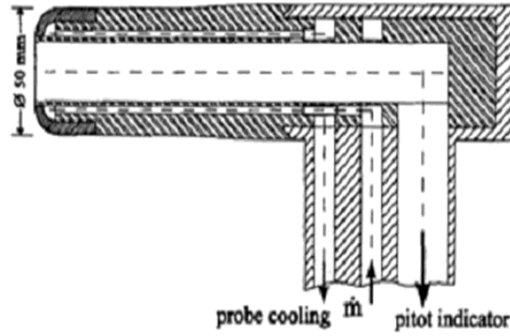


Figure 1.5: Schematic of Pitot probe

Flow velocity

Pitot probe With the measurements of total pressure by Pitot probes, Mach number can also be estimated. The relationship between pressure ration and Mach number is expressed as,

$$\frac{p_{\text{pitot}}}{p_{\text{amb}}} = \left(1 + \frac{\gamma - 1}{2} M^2 \right)^{\frac{\gamma}{\gamma - 1}} \text{ for a subsonic flow,} \quad (1.4)$$

$$\frac{p_{\text{pitot}}}{p_{\text{amb}}} = \left\{ \frac{(\gamma + 1)M^2}{2} \right\}^{\frac{\gamma}{\gamma - 1}} \left\{ \frac{\gamma + 1}{2\gamma M^2 - (\gamma - 1)} \right\}^{\frac{1}{\gamma - 1}} \text{ for a sonic flow,} \quad (1.5)$$

Here, p_{pitot} , p_{amb} and γ represents total pressure, ambient pressure and ratio of specific heat.

1.3.2 Non-Intrusive methods

In non-intrusive method, besides emission spectrometry, various techniques have been developed with development of laser. These techniques are roughly classified into spectroscopy, a scattering method, an interference method, a transmission method, and a reflection method [7][12]. Since particles is seldom

ionizing in diagnostics of high enthalpy wind tunnels, techniques other than the spectroscopy which is the way of measuring electron density and electron temperature are difficult to apply. Therefore, this section describes spectroscopy. Spectroscopy is based on transition of the electron in an atom or a molecule accompanied with spontaneous emission, absorption and fluorescence. Spectroscopy is classified into emission spectrography, laser absorption spectroscopy, and laser induction fluorescence by each transition. Each measuring method is described in detail later. Moreover, the merit and demerit of these techniques were summarized to Table 1.3.

Table 1.3: Comparison of LAS,ES and LIF

		LAS	textbfES(FPI)	textbfLIF
Optically plasma	thick	Applicable	Inapplicable	Inapplicable
Calibration		No need	Absolute light source	Reference cell
Portability		Easy	Possible	Impossible
Equipment		Not expensive	Expensive	Very expensive
Wavelength resolu- tion		<1pm	~0.1nm	<1pm

Table 1.4: Diagnostic method

Parameter	Intrusive method	Non-Intrusive method
Specific enthalpy	1.Energy balance 2.Enthalpy probe 3.Sonic flow 4.Stagnation point heat transfer	1.Translational temperature, flow velocity and species density (LAS, LIF, FPI)
Heat Flux	1.Gardon gage 2.Slug calorimeter 3.Radiometer probe	-
Flow velocity	1.Pitot probe 2.Mach probe 3.Time of flight probe	1.Doppler shift(LAS, LIF, FPI)
Stagnation pressure	1.Pitot pressure probe	
Species density	1.Mass spectrometer 2.Solid state electrolyte probe	1.LAS 2.LIF with a reference cell 3.CARS(Raman scattering)
Electron density and temperature	1.Electrostatic probe 2.Plasma absorption probe	1.ES with computation 2.Stark effect (ES, LAS, LIF, FPI) 3.Thomson scattering 4.Interference (Mach-Zehnder, etc.)
Excitation temperature	-	1.ES
Translational temperature	-	1.Doppler broadening (LAS, LIF, FPI)
Rotational and vibrational temperature	-	1.Molecular band (ES, LAS, LIF) with/without computation

1.4 Objectives

The following two improving points are mentioned to the past research as Section 3.3 shows.

- The solid state laser medium whose internal loss is generally smaller than a semiconductor laser is used.
- The system which suppresses mode-hopping and can sweep laser wavelength is developed.

In this research, the former point was set as the objective among these improving points, and the following steps were prepared.

1. The fundamental experiment Cr:LiSAF laser
2. The oscillation experiment of Cr:LiSAF laser with long laser cavity
3. The experiment of intracavity absorption spectroscopy with Cr:LiSAF laser

Chapter 2

Laser absorption spectroscopy for diagnosing high enthalpy flow

This chapter presents a theory of Laser absorption spectroscopy applied to plasma wind tunnels, its experimental system and our past results.

2.1 Principle of Laser Absorption Spectroscopy

From the quantum theory, every material has the infinite, specific and discrete orbits of electron about an atomic nucleus. A transition of the electron from one state to another can take place by absorbing an incident laser beam whose energy corresponds to the difference between the two states. Fig.2.1 shows the situation.

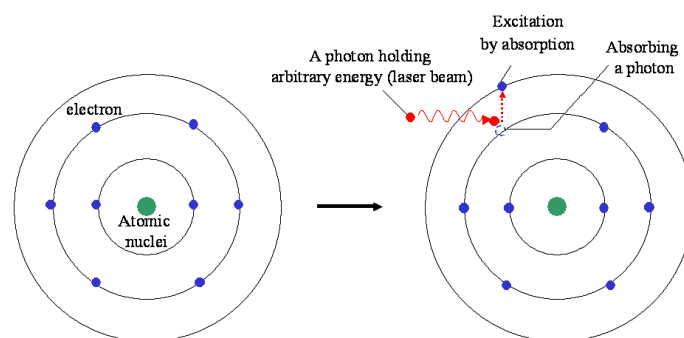


Figure 2.1: A transition of the electron by absorbing photon

Incident laser intensity is decreased by this absorption. The variation of laser intensity is showed in Fig.2.2. Reference signal showed the laser intensity which does not pass through an absorber, and absorption signal showed the laser intensity which passes through it. The absorption profile of atomic lines is derived from this variation of laser intensity (Fig.2.3). The profile has information such as its wavelength, intensity and shape. From such information, number density, translational temperature and flow velocity of the absorbing atom can be deduced. The relationship between these physical parameters and absorption profiles are illustrated in Fig.2.3.

In this section, application condition of laser absorption spectroscopy is discussed and the detail of the relationships described above is presented. Finally the measurement limit is considered.

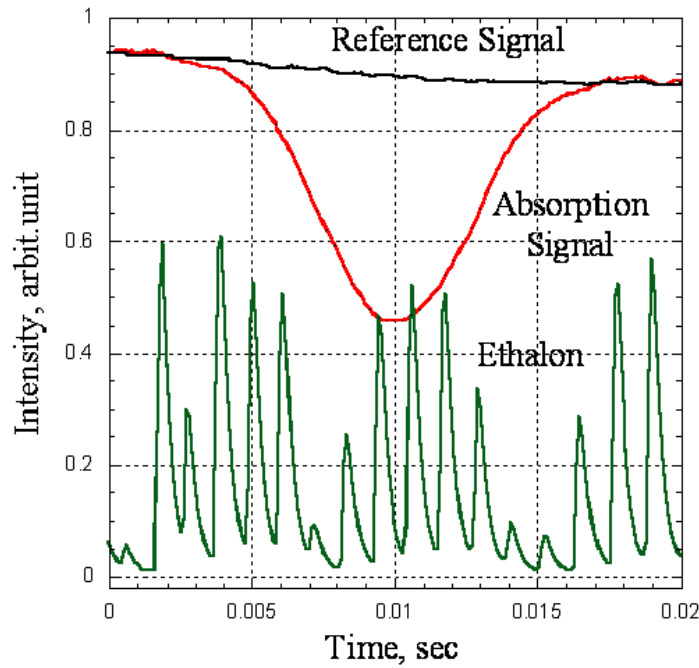


Figure 2.2: The variation of probe laser intensity

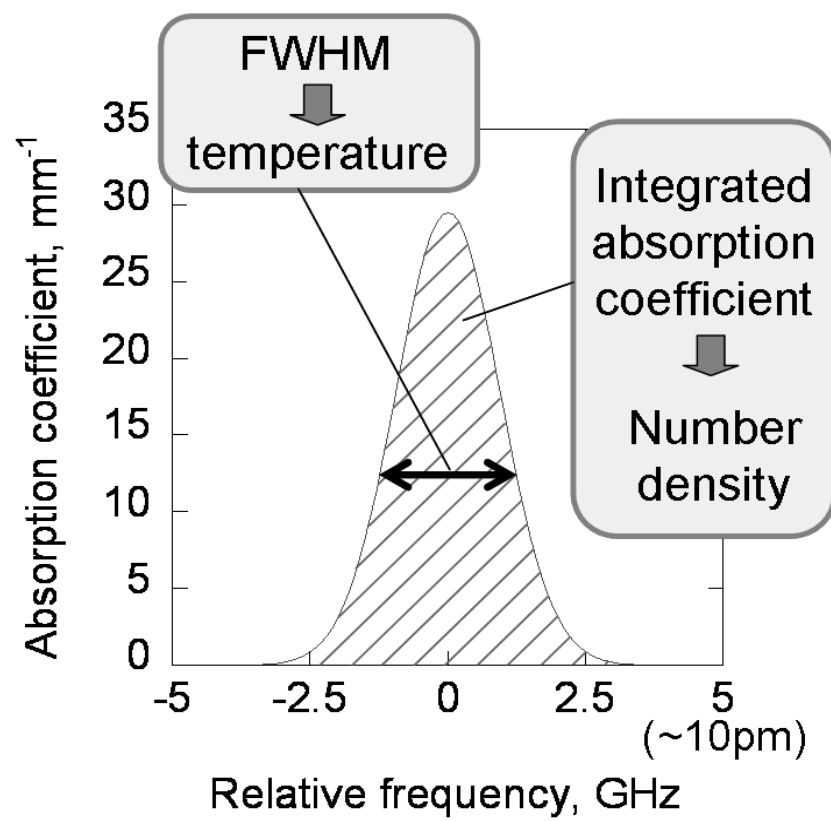


Figure 2.3: Absorption coefficient

2.1.1 Laser Absorption

The intensity variation dI of the probe laser with intensity I propagating through an absorbing sample is expressed by Beer-Lambert's Law,

$$\frac{dI}{dx} = -kx \quad (2.1)$$

Here, x and k are the optical pass length and absorption coefficient. The integration of (2.1) over the absorption path x gives the following formula (2.2),

$$\ln \frac{I_t}{I_0} = - \int k dx \quad (2.2)$$

Here, I_t and I_0 are the transmitting laser intensity and the incident laser intensity. For liner absorption, the absorption coefficient is expressed as,

$$k = -\frac{1}{L} \ln \frac{I_t}{I_0} \quad (2.3)$$

Here, L is the absorption pass length.

2.1.2 Broadning of absorption profile

Absorption profile of atomic line is broadened by various physical mechanisms, and is expressed by a convolution of the Lorentzian and the Gaussisan distributions. Here brief derivations and results are presented [13].

Doppler broadening

The proper frequency ν_0 of a moving atom at velocity v is observed to be shifted by the Doppler effect to

$$\nu_v = \nu_0 + \delta\nu \quad (2.4)$$

$$\delta\nu = \nu_0 \frac{v}{c} \quad (2.5)$$

Here, c is the velocity of light. Assuming that the velocity distribution of the atom obeys to the Maxwell distribution, the probability that the velocity component of the atom to the light direction is in $\nu + \Delta\nu$ is

$$p(\nu)d\nu = \left(\frac{M_A}{2\pi kT} \right)^{\frac{1}{2}} \exp \left(-\frac{M_A \nu^2}{2kT} \right) d\nu \quad (2.6)$$

Here, M_A is the atom mass, k is Boltzmann constant and T is the temperature. Therefore, a normalized profile is a Gaussian and expressed as,

$$g(\nu) = \frac{1}{\pi^{1/2} \Delta\nu_D} \exp \left\{ -\left(\frac{\nu - \nu_0}{\Delta\nu_D} \right)^2 \right\} \quad (2.7)$$

This is called the Doppler broadening. The full width at half maximum (FWHM) $\Delta\nu_D$ is related to the temperature as follows.

$$\Delta\nu_D = \frac{2\nu_0 \sqrt{\ln 2}}{c} \sqrt{\frac{2kT}{M_A}} = 7.16 \times 10^{-7} \sqrt{\frac{T}{M_A}} \nu_0 \quad (2.8)$$

Natural Broadening

Natural broadening is originated by the finite time of the transition. The Heisenberg uncertainty principle is expressed as,

$$\Delta E \cdot \Delta t \approx \hbar \quad (2.9)$$

Considering that the life time of the atom is $\Delta t = 1/A$, the uncertainty of the frequency is $\Delta\nu_N$ expressed as,

$$\begin{aligned} \Delta\nu_N &= \frac{\Delta E}{h} \\ &= \frac{A}{2\pi} \end{aligned} \quad (2.10)$$

This profile is the Lorentz type. Generally, typical A coefficient is from $10^7 \sim 10^8 s^{-1}$ [14]. Therefore $\Delta\nu_N$ is the order of $2 \sim 20\text{MHz}$.

Collision Broadening(Pressure Broadening)

The collision broadening is originated from the fact that atoms are perturbed by collisions with other atoms (or molecules). In the phenomenological treatment, two types of collisions are discussed. One is the collision-induced transition and the other is the phase-changing collision. In the former collision, if the energy difference between atomic levels is not very large compared with the kinetic energy of the colliding atom, the collision induces a transition between the atomic levels. In the latter one, phase of the state suffers a phase shift by collisions because the phase of atomic wave function is more frequently perturbed than is the population of the atomic level by collisions with other atoms. This profile is the Lorentzian and the FWHM of these broadening $\Delta\nu_C$ is expressed as, [13]

$$\Delta\nu_C = (C_1 + C_2 + 2C_{12})p \quad (2.11)$$

Here, p is the pressure, C_1 , C_2 are the parameters related to with the collision-induced transition, and C_{12} is the parameter related to the phase-changing collision. Values of these three parameters are experimentally found in the range from 1 to 30 MHz/torr depending on the kind of atoms (or molecules) and temperature.

Stark Broadening

Stark broadening originates from the fact that the degeneracy is solved by the electric field which a surrounding electron makes. This profile is the Lorentz type and is expressed as, [13]

$$\Delta\nu_S = 1.0 \times \left\{ 1 + 1.75 \times 10^{-4} n_e^{1/4} \alpha \left(1 - 0.068 n_e^{1/6} T_e^{-1/2} \right) \right\} n_e w \cdot 10^5 \quad (2.12)$$

Here, w is electron impact parameter, α is ion-broadening parameter, n_e is electron density, and T_e is electron temperature.

Saturation Broadening

Saturation broadening is originated from the increase in the line width with the optical field intensity by the nonlinear effect as described in section 2.1.1. This profile is the Lorentz type and the broadening $\Delta\nu_P$ is expressed as,

$$\Delta\nu_P = \frac{1}{\pi} \sqrt{\gamma^2 + |x|^2} \quad (2.13)$$

Here, γ is the reciprocal of the mean collision time and $|x|$ is the Rabi frequency.

However, absorption saturation was found to cause the more broadening than that described above [15].

Transit-time Broadening

Transit-time broadening is originated from the transit of the particles through light beam. This profile is Lorentz type and the broadening $\Delta\nu_T$ is expressed as, [14]

$$\Delta\nu_T = \frac{v}{2\pi a} \quad (2.14)$$

Here, v is the velocity of the atom and a is the beam diameter.

$$*\Delta\nu_s = 1.0 \times \left\{ 1 + 1.75 \times 10^{-4} n_e^{1/4} \alpha \left(1 - 0.068 n_e^{1/6} T_e^{-1/2} \right) \right\} n_e w \cdot 10^5$$

Table 2.1: Comparison of broadening effects

Broadening	origin	FWHM	Typical Value
Doppler	Thermal motion of atoms and molecules	$\frac{2\nu_0\sqrt{\ln 2}}{c}\sqrt{\frac{2kT}{M_A}}$	$\sim 2.2\text{GHz}(\text{Oxygen } 1000\text{K})$
Natural	Finite time of transition	$\frac{A}{2\pi}$	$\sim 1.6\text{MHz}(A=10^{-7}\text{s}^{-1})$
Collision	Interparticle collision	$(C_1 + C_2 + 2C_{12})p$	$\sim 10\text{MHz}(0.1\text{ torr})$
Stark	Electric field	*	$\sim 36\text{MHz}(\text{Oxygen Ne}=20\text{m}^{-3})$
Saturation	Absorption saturation	$\frac{1}{\pi}\sqrt{\gamma^2 + x ^2}$	$\sim 10\text{MHz}(10\text{mW})$
Transit-time	Transit of particles through the laser beam	$\frac{\nu}{2\pi a}$	$\sim 1\text{kHz}(\alpha = 1\text{mm})$

2.1.3 The way of estimating physical parameters of high enthalpy flow

Integrated absorption coefficient and number density

Integrated absorption coefficient is defined as,

$$K = \int_{-\infty}^{+\infty} k(\nu) d\nu \quad (2.15)$$

Here, K is integrated absorption coefficient, $k(\nu)$ is absorption coefficient. Assuming that laser absorption consists of absorption and induced emission, the total absorption is expressed as,

$$k(\nu) d\nu = \frac{h\nu}{c} (B_{ij} dn_i - B_{ji} dn_j) \quad (2.16)$$

Here, n_i is lower state number density, n_j is the upper state number density, B_{ij} , B_{ji} is the Einstein B coefficients. Substituting the following relationship between A and B coefficients,

$$\begin{aligned} A_{ij} &= \frac{8\pi h\nu^3}{c^3} \frac{g_i}{g_j} B_{ij} \\ &= \frac{8\pi h\nu^3}{c^3} B_{ji} \end{aligned} \quad (2.17)$$

to the equation (2.16), the integrated absorption coefficient is expressed as,

$$\begin{aligned}
K &\equiv \int_{-\infty}^{+\infty} k(\nu) d\nu \\
&= \frac{c^3}{8\pi h \nu^3} \frac{g_j}{g_i} A_{ji} n_i \left(1 - \frac{g_i}{g_j} \frac{n_j}{n_i} \right)
\end{aligned} \tag{2.18}$$

Assuming the Boltzmann equilibrium between n_i and n_j states, n_i is related to n_j as,

$$n_j = \frac{g_j}{g_i} n_i \exp \left(-\frac{\Delta E_{ij}}{k T_{\text{ex}}} \right) \tag{2.19}$$

Here, ΔE_{ij} is the energy between n_i state and n_j state, k is Boltzmann constant and T_{ex} is the electron excite temperature. From the equations (2.18) and (2.19), the following relationship is obtained.

$$K = \frac{\lambda^2}{8\pi} \frac{g_j}{g_i} A_{ji} n_i \left\{ 1 - \exp \left(-\frac{\Delta E_{ij}}{k T_{\text{ex}}} \right) \right\} \tag{2.20}$$

In our research, $\Delta E_{12}/k$ corresponding to oxygen 777.19 nm and argon 840.82 nm absorptions is about 20,000K. This is much smaller than T_{ex} . Therefore, the integrated absorption coefficient is expressed as follows.

$$K = \frac{\lambda^2}{8\pi} \frac{g_j}{g_i} A_{ji} n_i \tag{2.21}$$

Here, if absorption coefficient $k(\nu)$ is approximated by Gaussian profile, it is expressed as follows

$$k(\nu) = k(\nu_0) \exp \left\{ -\left(\frac{\nu_0 - \nu}{\Delta \nu_D} \right)^2 \right\} \tag{2.22}$$

Therefore, integrated absorption coefficient K is expressed as follows

$$K = \int_{-\infty}^{+\infty} k(\nu) d\nu = \sqrt{\pi} k(\nu_0) \Delta \nu_D \tag{2.23}$$

Here, $\Delta \nu_D$ is Doppler broadening.

Flow temperature

As mentioned in 2.1.2 Doppler broadening, the flow temperature is related to the Doppler broadening $\Delta \nu_D$ as (2.8).

Flow velocity

The absorption wavelength of the moving atom in a direction shifts by the Doppler effect. Therefore, from the shift quantity and the angle between the moving direction and the laser beam, the flow velocity is obtained by the following relationship.

$$V = \frac{\Delta\nu \cdot \lambda_0}{\cos\theta} \quad (2.24)$$

Here, V is the flow velocity, $\Delta\nu$ is the shift quantity, λ_0 is the absorption wavelength of the atom at rest and θ is the angle between the flow direction and laser beam.

2.1.4 Absorption Target

In this research, the target absorption lines are the transition from the metastable oxygen ($3s^5S$) and argon ($4s^2[1/2]$). This is because number density of metastable states is much larger than other excited states one, so that it is easy to detect the absorption profiles. The transition data of these lines and their Grotrian diagrams are shown in Table 2.2 and Fig 2.4 and 5 [14].

Table 2.2: Transition data

	1	2	λ (nm)	E_1 (eV)	E_2 (eV)	g_1	g_2	A_{21} ($10^8 s^{-1}$)
OI	$3s^5S$	$3p^5P$	777.19	9.15	10.74	5	7	0.369
OI	$3s^3S$	$3p^3P$	844.62	9.52	10.99	3	1	0.322
OI	$3s^3S$	$3s^3S$	844.64	9.52	10.99	3	5	0.322
ArI	$4s^2[1/2]$	$4p^2[3/2]$	840.82	11.62	13.09	3	5	0.223
ArI	$4s^2[3/2]$	$4s^2[5/2]$	842.46	13.28	14.74	3	5	0.215
ArI	$4s^2[1/2]$	$4s^2[2/2]$	852.14	11.62	13.28	3	3	0.139

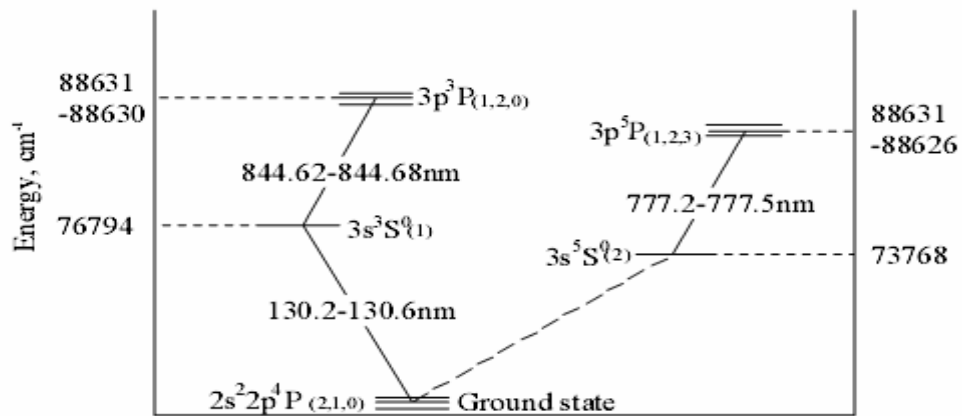


Figure 2.4: Grotrian diagram of atomic oxygen

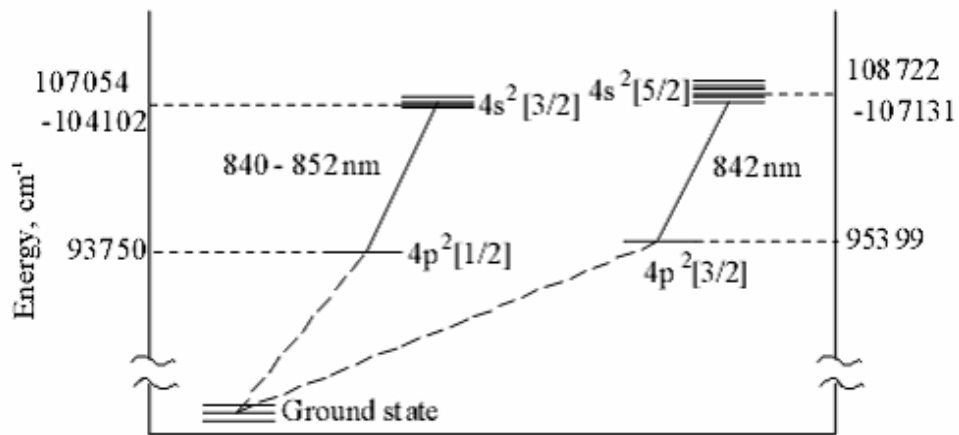


Figure 2.5: Grotrian diagram of atomic argon

2.2 Measurement system

In our past research, diagnostics for plasma generating by argon discharge tube and arc heater have been done by laser absorption spectroscopy. Experimental system of argon discharge tube and arc heater is shown in Fig.2.6 and Fig.2.7, respectively.

In the experiment of argon discharge tube, laser beam oscillated external cavity diode laser (ECDL) was passed through an isolator and divided by a beam splitter into probe beam, reference beam and etalon beam. Probe beam was passed through ND filter, argon discharge tube and band pass filter, and detected by photo detector. Etalon beam was passed through an etalon, and detected by photo detector. Reference beam was directly detected by photo detector. Detected beams were recorded by oscillo scope.

In the experiment of arc heater, laser beam oscillated ECDL was divided into three beams as well as the case of argon discharge tube. The probe beam was entered into an optical fiber because the distance between an optical bench and vacuum chamber which has the arc heater into itself is a little long. And then, probe beam was passed through a collimating lens, which was attached to exit of an optical fiber, and an arc plume in a vacuum chamber, focused by a parabola mirror, passed through a band pass filter, and detected by a photo detector. In a measurement of a space distribution of an arc plume, spatial positioning was doing by controlling two axis stepping motor which an optical fiber is attached to.

The optical components used in the systems are explained in the following sections.

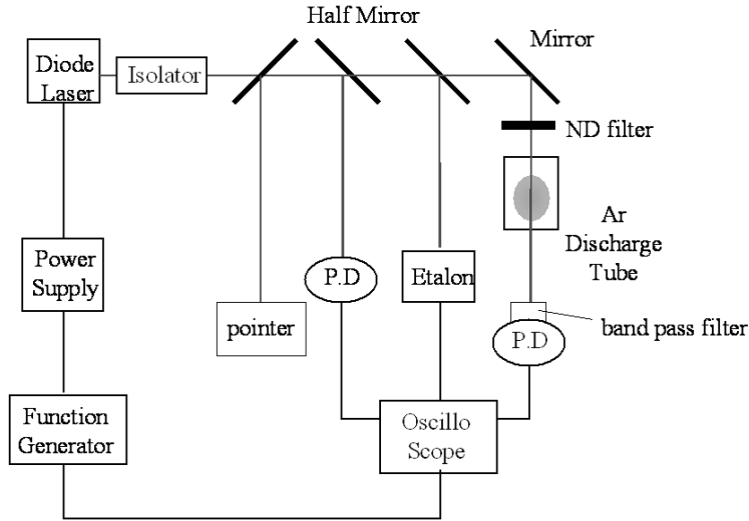


Figure 2.6: Schematic of the optical system for Ar discharge tube

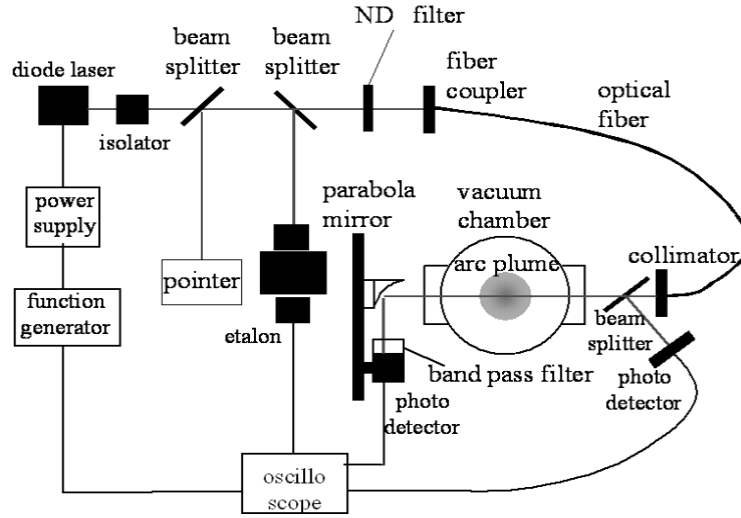


Figure 2.7: Schematic of the optical system for arc heater

2.2.1 External cavity diode laser (ECDL)

There were two ECDLs used in the experiment systems. One is External Cavity Diode Laser Model 2010 (Environmental Optical Sensors, Inc) and the other is Velocity Model 6300 (Indeco, Inc).

These lasers are composed of diode laser and diode laser controller. Diode laser is mounted with a collimating lens, thermistor for controlling temperature, Peltier element, and external cavity for modulating wavelength. This laser and laser controller are compact system, and a wavelength of the laser is modulated only by connecting function generator.

The oscillating wavelength of EOR Model 2010 and Velocity Model 6300 is 840~860nm and 760~780nm, respectively. The advantages of these lasers are a wide tuning range, modulating laser wavelength smoothly and almost mode-hop free in the tuning range. In addition, the output power is stable because injection current of the lasers is maintained a constant value. Maximum output power of EOR Model 2010 and Velocity Model 6300 is 20mW and 10mW, respectively.

A mechanism of External cavity and oscillation principle are explained in chapter 4.

2.2.2 Isolator

In the experiment system, the isolator (I-80-U4, ISOWAVE) was used in order to prevent the scattering laser beam from returning into the laser cavity and becoming a noise source. This isolator is developed at 800nm. The figure of the isolator is shown in Fig. 2.8. The Faraday rotator F which is inserted between

polarizer P1 and P2, placed into an apertured permanent magnet, and applied a magnetic field to the laser beam direction. This magnetic field is applied to make magnetic domains of the Faraday rotator a single domain. As shown in Fig.2.8, figure, incident laser beam is made into linear polarization by polarizer P1, and passes through the Faraday rotator F. Incidence linear polarization is rotated 45 degrees, only the component of 45 degrees from vertical can pass through P2. This polarization component is rotated more 45 degrees by the Faraday rotator F, and become the polarization which is rotated 90 degrees to the direction of transmission of P1. Therefore, laser beam does not return to the laser cavity.

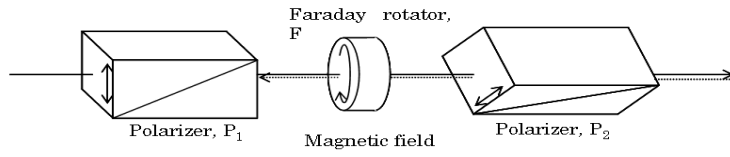


Figure 2.8: Block diagram of isolator

2.2.3 Etalon

In absorption spectroscopy, an etalon signal becomes the standard data for transforming a time series data into frequency. Etalon is a cavity built in the confocal mirror which faces each other. When a laser beam enters into etalon and the wavelength becomes an integral multiple of the cavity length of an etalon, it transmits and is detected by the detector of the opposite side. Then, a fringe-like signal is observed with tuning wavelength. the free spectral range (FSR) depends on the cavity length. In the experiment system, the etalon (Neo Arc.inc) whose FSR is 1GHz, was used. The principle of an etalon is as follows. The feature of etalon is shown in Fig.2.9.

This is the figure that it is reflected in a B point and the laser beam which entered from A point is reflected at B point, and further done at C point. Here, the case where a laser beam enters perpendicularly is considered. When cavity length, which is an interval of a mirror and a mirror, is set to t , the condition which incident light and reflected light resonate is as follows.

$$p = \frac{2t}{\lambda} \quad (2.25)$$

Here, p is an integer (order) and λ is a wavelength of a laser beam. The cavity length should just be an integral multiple of the wavelength of a laser beam. p is an integer (order) and λ is a wavelength of

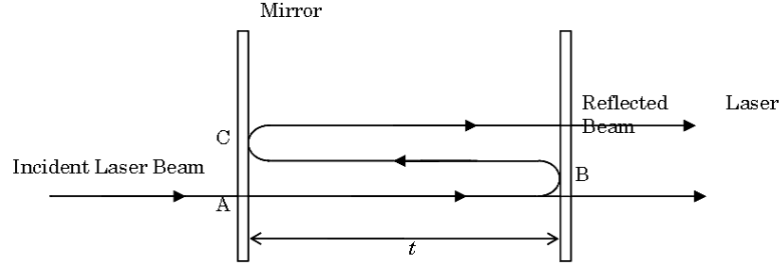


Figure 2.9: The principle feature of an etalon

a laser beam here. The cavity length should just be an integral multiple of the wavelength of a laser beam. When the wavelength of a laser beam is changed little by little, resonance is caused next in the following cases.

$$p + 1 = \frac{2t}{\lambda + \Delta\lambda} \quad (2.26)$$

If these formulas are allied, the following relations will be obtained.

$$\frac{\Delta\lambda}{\lambda^2} = \frac{1}{2t} = \text{const} \quad (2.27)$$

Here, the condition which is $2t \gg \lambda$ is used. On the other hand, the speed of light, the wavelength of light, and frequency of the relations is as follows.

$$c = \nu\lambda \quad (2.28)$$

Here, c is the speed of light, and ν is frequency of light. If the wavelength of a laser beam is changed $\Delta\lambda$ and the frequency is done $\Delta\nu$, the formula (2.28) is as follows.

$$c = (\nu + \Delta\nu)(\lambda + \Delta\lambda) \quad (2.29)$$

The following relations will be obtained if (2.28) and (2.29) are allied.

$$\Delta\nu = \frac{\Delta\lambda}{\lambda^2}c \quad (2.30)$$

It is found that the left hand side of (2.30) takes constant value from (2.27). Therefore, an etalon will cause resonance for every constant frequency, and will output a signal.

2.2.4 Photo detector

In order to measured laser intensity, High Speed Detector Package (DET1-S1/M and DET110, THOR-LABS.inc) were used. Moreover, the light of a fluorescent is detected by a photo detector, and it becomes noise because a photo detector has high sensitivity. Therefore, in the experiment, a band pass filter (the center wavelength 840nm) was attached to the front of a photodetector.

2.2.5 Function generator

In the experiment system, the function generator (AFG310, SONY TEKTRONIX.inc) was used. It changes continuously the voltage applying the piezo element for tuning laser wavelength. The change of voltage was outputted as a triangular wave to detect the broadening of absorption profile.

2.2.6 Power meter

The power meter (TQ8210, ASVANTEST) was used to measure laser power. Detection element is a silicon photo diode. A photodiode is a photo acceptance unit using the character which photoelectromotive force generates, when light strikes upon the connection of PN junction diode. The current is proportional to intensity of light and the response speed is quick. As a result, light intensity can be measured with ± 5 percent of measurement accuracy in the range of 400-1700nm.

2.2.7 Argon glow discharge tube

In the experiment system, the argon glow discharge tube (CI techno) was used as a test plasma for performing absorption spectroscopy. The outline view of an argon discharge tube is shown in Fig.2.10. Into this glass tube, argon gas (0.5torr) is enclosed, and argon plasma is generated by applying the voltage of about 200v between the cylindrical metals located in the central part of the glass tube. Because of glow discharge, the current is 1mA~3mA, and the power is 0.2W~0.6W. The size of this discharge tube is 8.5cm in length, 3cm in diameter. In addition, since the quality of the material of this glass tube had to be a thing which can be transmitted by the laser beam near near-infrared for the plasma measurement, BK7 and Pyrex

were used. In the experiment of a discharge tube, since the glass surface becomes black by sputtering as an experiment is repeated, an electrode is good to locate in the center of a glass tube as much as possible. Thereby, a laser beam transmits and a life time of a discharge tube also becomes long. The life time is from half a year to one year generally. Fig. 2.11 shows the appearance of the discharge tube under operation.

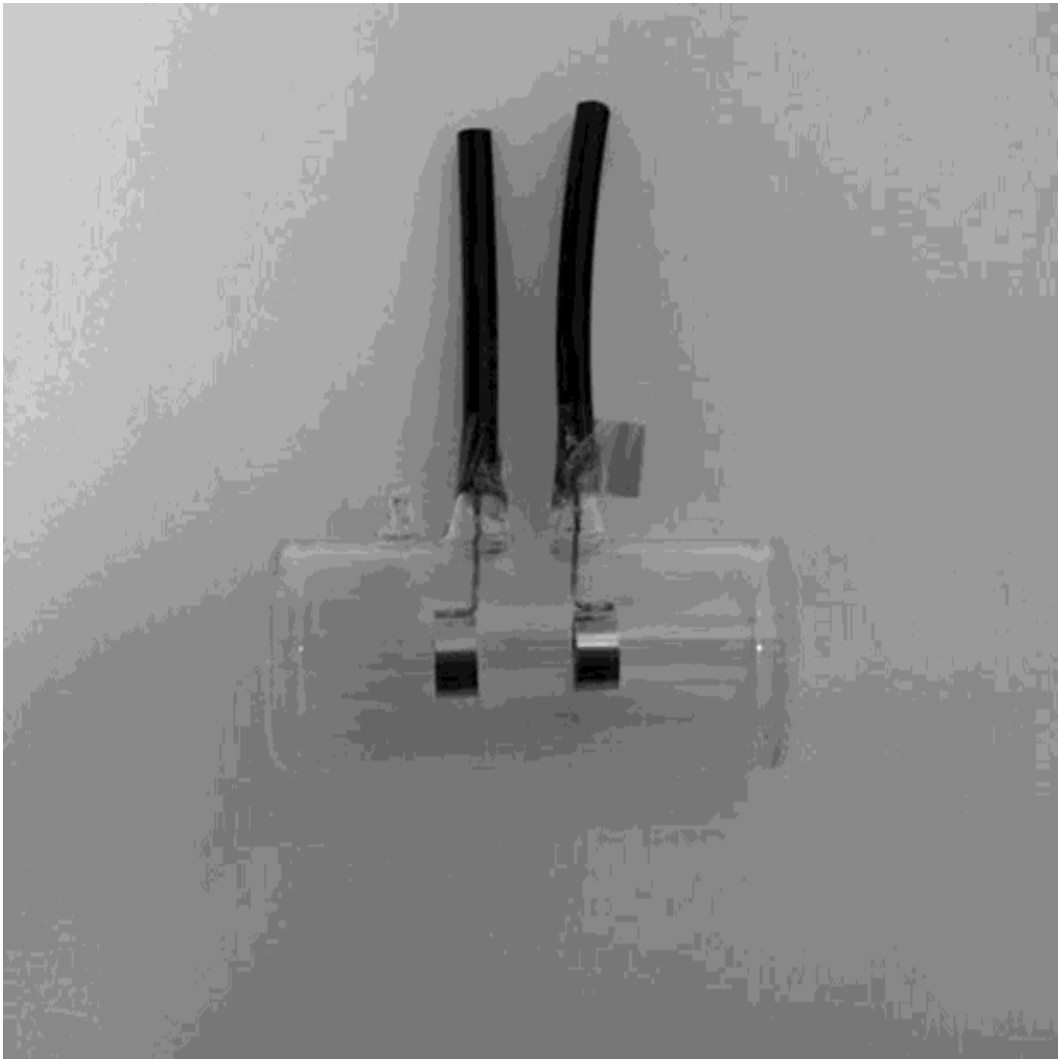


Figure 2.10: Arc discharge tube

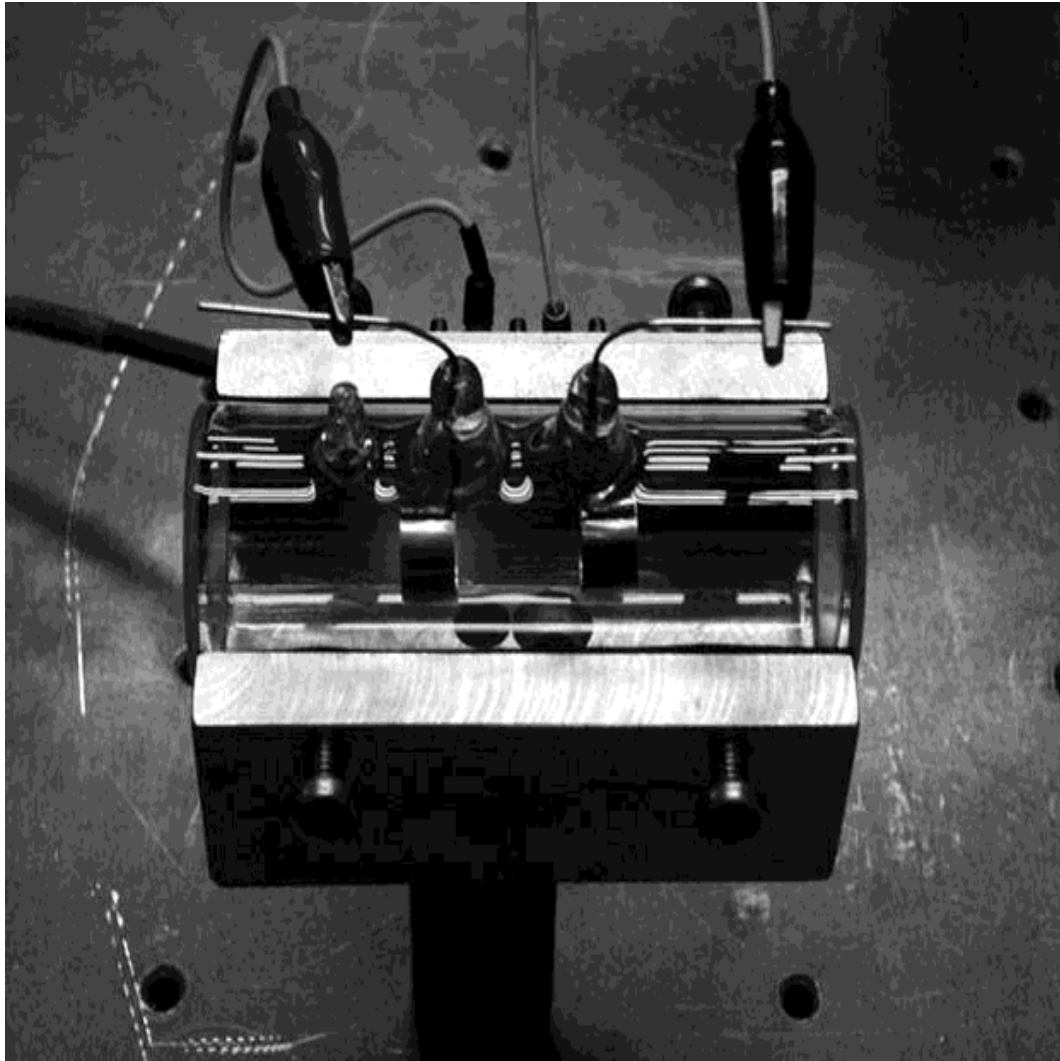


Figure 2.11: Ar discharge tube on operating

2.2.8 Arc heater

Fig.2.12 shows the outline view of the arc heater developed in the University of Tokyo. Moreover, the cross section view is shown in Fig.2.13. The cathode of this arc jet is made of thoriated tungsten which has high thermostability, and the anode is made of copper. Arc discharge is caused among both electrodes and plasma is generated.

The ignition procedure of an arc heater is described. Argon is first supplied from the lower stream and it is ignited by an ignitor. Then, oxygen is supplied from the part which is before the constricted part of a nozzle, and the plasma is generated in an argon/oxygen flow because the tungsten cathode is deteriorated by oxidization and it is impossible to generate plasma. Since energy is used for dissociation of oxygen and it will be very hard to generate plasma if oxygen is supplied first, such a procedure is taken. In order to simulate the reentry environment more correctly, not argon but nitrogen must be used. However, if nitrogen is used instead of argon, it is difficult to generate plasma. Since the main cause of the thermostability material wastage at the time of reentry is the catalysis of an atomic oxygen, the point of supplying nitrogen has been compromised on this research. If plasma is generated in a nitrogen-oxygen flow, a power source which can supply more bigger than electric power than one supplied in this research can be needed. It is hard to generate plasma because the tip of tungsten is oxidized and becomes blackish after the operation. Therefore, after the operation, the maintenance of the cathode must be done.

An anode and cathode are cooled by cooling water. Cooling water and Gas, such as argon and oxygen, is supplied to an arc heater from the straight with hexagon socket (POC6-01M mini type, PISCO) shown in Fig.2.12. cooling water is supplied from the cooling tower installed in the outside of our laboratory. This cooling tower is NT-1014 (Hitachi Cold). As for the performance, volume of water is 130 l/min, and the cooling capacity is 45.3kW (39000 kcal/h). Moreover, supply gas, such as oxygen and argon, is made by Joto gas. These are contained in the gas cylinder which can be borne to 150 atmospheric pressure, and go into a massflow controller through a tube. The massflow controllers for argon and oxygen are MODEL 3610, MODEL3620, etc.(KOFLOC), and the lead-out unit for setting them up is CR700A etc.(KOFLOC). Full scale of the massflow controller of argon and oxygen are 20slm and 10slm, respectively.

The operating conditions of an arc heater are shown in Table 2.3. The thermal efficiency shown in this table is referred from the past data. Moreover, specific enthalpy is obtained by dividing injection power about 1kW by a gas mass flow, and multiplying it by heat efficiency.



Figure 2.12: Arc heater made in Tokyo University

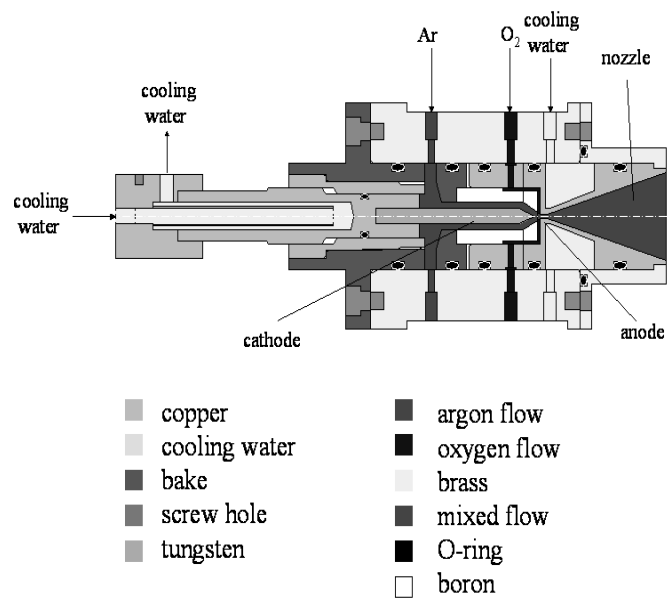


Figure 2.13: Cross section view of the arc heater made in Tokyo University

Table 2.3: Operating conditions of the arc heater

Voltage	15~20V
Current	50~60A
Thermal efficiency	0.56
Specific enthalpy	3.36MJ/kg
Mass flow rate of argon	6slm
Mass flow rate of oxygen	0.5slm

2.3 Past results

In this laboratory, various plasma wind tunnels have been measured in the absorption line (840.82nm, 842.46nm) of argon, and the absorption line (777.19nm) of oxygen [16] using the laser absorption spectroscopy . The result was summarized to Table 2.4.

Table 2.4: Previous measurement for various plasma wind tunnels

Wind Tunnel	Facility	Input power	Ar-O ₂ uniform flows	O ₂ uniform flows	N ₂ -O ₂ (Air) flows	N ₂ -O ₂ (Air) Shock
Arc Heater (Arcjet)	Univcity of Tokyo	1kW	Yes	-	No	No
Arc Heater (Arcjet)	JUTEM	20kW	Yes	-	No	Weak
Arc Heater (Segment)	ISTA/JAXA	750kW	-	-	No	No
Arc Heater (Segment)	ISAS/JAXA	1MW	-	-	No	No
ICP	Stuttgart	100kW	-	-	No	-
ICP	ISTA/JAXA	100kW	-	-	No	No

As shown in Table 2.4, in the pure oxygen flow (ICP), and argon/oxygen flow (Arc wind tunnel), the strong absorption signal of the atomic oxygen line (OI: 777.19nm) was detected [17]. However, in nitrogen/oxygen flow, the absorption signal could not be detected in the arc wind tunnel, except for the absorption signal was slightly detected in ICP [18]. The absorption profile in a pure oxygen flow, and nitrogen/oxygen flow are shown in Fig. 2.14. In N/O flow, although specific enthalpy was 130kW which is higher than 110kW of a pure oxygen flow, the absorbance became 0.045.

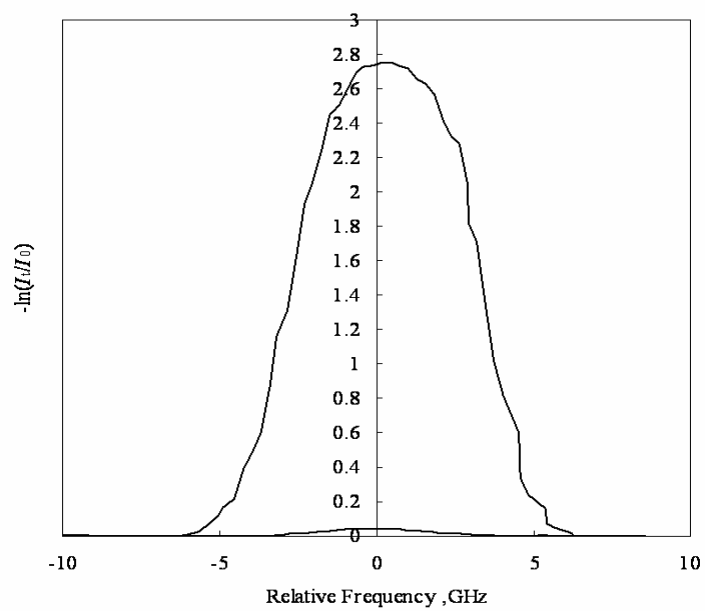


Figure 2.14: Absorbance in pure oxygen and nitrogen/oxygen flows of IRS

Chapter 3

High sensitivity laser absorption spectroscopy

3.1 High sensitivity laser absorption spectroscopy

The sensitivity of laser absorption spectroscopy can be enhanced by extending an optical absorption path length from a formula (2.3). Some methods shown below as the technique of extending the optical absorption path length are proposed.

3.1.1 Free propagation of light in the atmosphere

Free propagation of light in the atmosphere [19] provides up to 16km absorption length. Such long-path measurements, however, apply only to atmospheric extinction and merely provide an average over the entire absorber length.

3.1.2 Multireflection cells

Multireflection cells [20] allow some 100 fold extension of the effective absorber length. This factor is limited by the loss of light at the mirrors, and by the necessity of sufficient geometrical separation of the successively reflected laser beams. With 10m base length of the cell, the effective absorption length may be at most 1km.

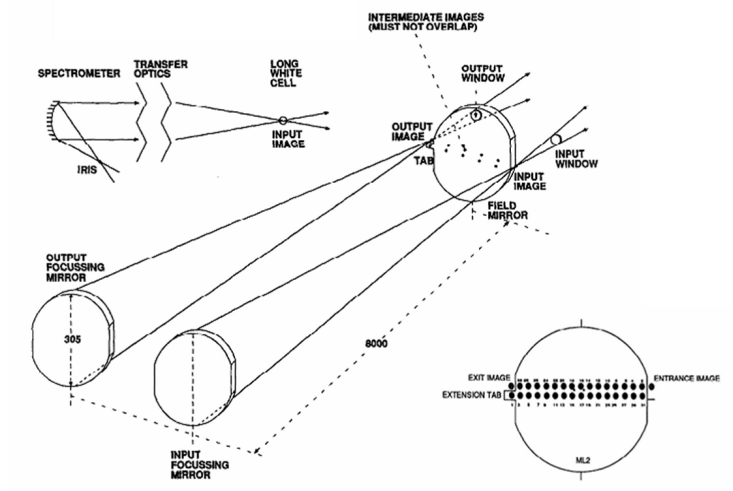


Figure 3.1: Schematic diagram of the long white cell optics and the interface to the spectrometer

3.1.3 Cavity ring down spectroscopy (CRDS)

Higher enhancement of the effective absorption path length is accomplished by the method of cavity ringdown spectroscopy [21]. Here, the absorber is placed inside a passive cavity, into which a short laser pulse is injected (Fig.3.1).

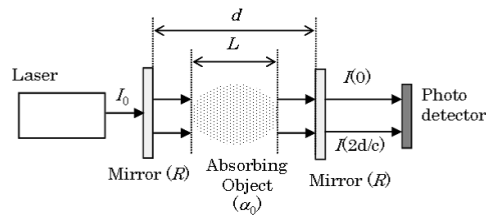


Figure 3.2: Schematic for principle of cavity ring down laser absorption spectroscopy

If an incidence laser whose intensity is I_0 is detected without reflection, the transmission intensity is as follows.

$$I(0) = I_0(1 - R^2) \exp(-\alpha_0 L) \quad (3.1)$$

If it is reflected twice, the transmission time Δt is,

$$\Delta t = \frac{2d}{c} \quad (3.2)$$

Here, c is light speed. At that time, the transmission intensity is,

$$I\left(\frac{2d}{c}\right) = I(0)R^2 \exp(-2\alpha_0 L) \quad (3.3)$$

Furthermore, the transmitted laser reflected one by one is detected behind time. Decay factor of the transmission intensity is expressed as following formula.

$$\tau = \frac{d}{c(|\ln R| + \alpha_0 L)} \quad (3.4)$$

Therefore, to the decay factor τ_0 in case there is no absorber,

$$\tau_0 = \frac{d}{c|\ln R|} \quad (3.5)$$

if $\alpha_0 L$ is as follows, the decay by absorption of an absorber can be detected and the density of an absorber can be obtained.

$$\alpha_0 L \approx |\ln R| \approx 10^{-3} (R = 99.9\%) \quad (3.6)$$

However, a slight change of the reflectivity R under measurement also influences the decay greatly. The effective absorption length is determined by the reflectivity of cavity mirrors, and by the cavity length L .

3.1.4 Cavity enhanced absorption spectroscopy (CEAS)

A CW laser is used as a light source although CEAS is the same system as CRDS [22]. Its cost is low by this, and transmitted laser intensity in CEAS is greatly larger than CRDS because a laser beam is resonated in the cavity. Therefore it is easy to detect. Moreover, time resolution of CEAS is better than CRDS since a CW laser is used.

In CEAS, only a laser beam whose frequency meets the resonance condition can transmit the cavity. Then, the absorption signal is obtained through integration of the total signal transmitted through an optical cavity. The integrated transmitted signal as the summation as follows,

$$I = I_0 T^2 \sum R^{2n} \exp\{-(2n+1)k_\nu d_0\} \quad (3.7)$$

Where n is the number of reflections in the cavity. The summation can be approximated by an integral over n (for large n) resulting in as follows

$$I = I_0 T^2 \exp(-k_\nu d_0) \int_0^\infty \{R \exp(-k_\nu d_0)\}^{2n} dn \quad (3.8)$$

Solving this expression, following equation is obtained.

$$\frac{I}{I_0} \approx (1 - R)^2 \frac{\exp(-k_\nu d_0)}{-2 \ln R \exp(-k_\nu d_0)} \quad (3.9)$$

Here the mirror loss is neglected. It depends for the absorption sensitivity in CEAS on the reflectivity of a cavity mirror like CRDS.

3.1.5 Intracavity absorption spectroscopy (ICAS)

The principal features of ICAS are shown in Fig.3.2 [23].

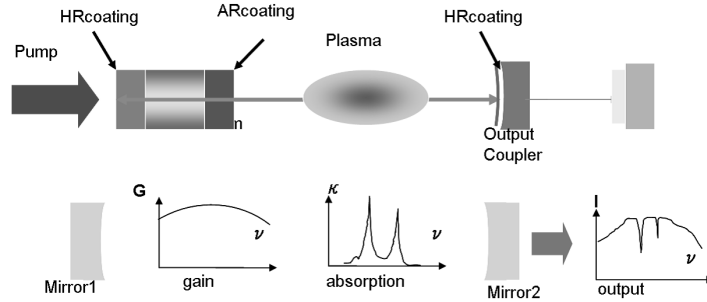


Figure 3.3: Schematic for principle of intracavity absorption spectroscopy

The laser cavity consists of two mirrors M1 and M2 and includes a medium of broadband gain $G(\nu)$ and a sample with a narrow-line absorption spectrum $\kappa(\nu)$. The sample is either confined in an absorption cell, or just placed in an open part of the cavity. The foremost requirement for the application of multimode ICAS is that the linewidth of the absorber is smaller than spectral broadening of the gain medium. Although the laser gain is made to compensate broadband cavity loss such as the mirror transmission, it is not affected by narrow-line ICA. The laser light passes through the absorber many times, and ICA is accumulated in its spectrum, as in a multipass cell.

The experiment has been performed using various lasers . They are shown in Table 3.1.

Table 3.1: Intracavity absorption spectroscopy by several laser types

Laser type	t_s (ms)	L_{eff} (km)	Limitation	$\Delta\nu_{\text{exp}}$ (GHz)
Dye	230	70000	FWM	45
Ti:sapphire	4.5	1300	FWM,RS	100
Diode	0.13	40	SE	3
Fibre	0.43	130	RS	1500
Nd ³⁺ -glass	12	3600	τ	300
CCL	0.4	120	τ	3000
OPO	5×10^{-6}	0.0015	τ	200

The values of spectral saturation time t_s of absorption, effective absorption path length L_{eff} and the emission bandwidth $\Delta\nu_{\text{exp}}$ (HWHM) achieved in ICAS measurements with various lasers. The origin of the limitation of sensitivity is indicated as FWM for four-wave mixing, RS for Rayleigh scattering, SE for spontaneous emission, and τ for limitation by the laser pulse duration. The detailed principle of intracavity absorption spectroscopy is expressed in next section.

3.2 Principle of intracavity absorption spectroscopy

3.2.1 Laser threshold power and output power

Rate equation

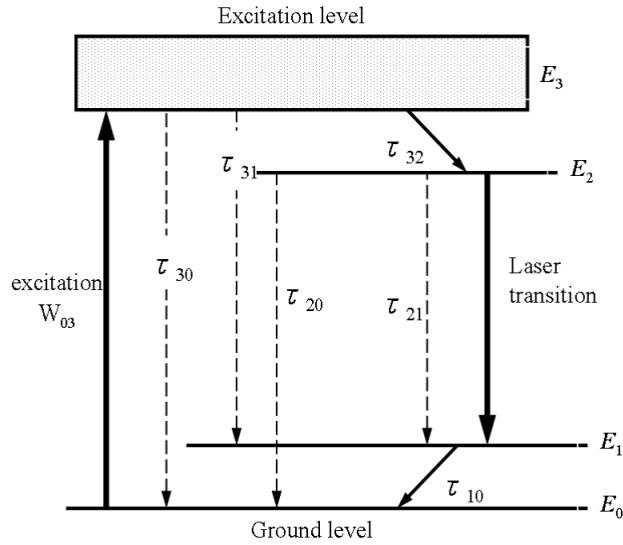


Figure 3.4: Schematic for energy level of four level laser

Ideal four level laser as shown in Fig.3.3 is considered. In this case, to the ground level E_0 , the energy E_1 of the laser lower level is large enough, $E_1 \gg kT$ is realized at the operation temperature T , and the thermal excitation to the lower level is lost. Furthermore, if the lifetime of the level 3 is much shorter than other levels, the distribution density of a level 3 can be neglected. The temporal change of the distribution density of each atomic level becomes like the following formula from these conditions.

$$\frac{dN_2}{dt} = W_p N_0 - N_2 - (g_2/g_1) N_1 \sigma_{21} c \phi - \frac{N_2}{\tau_{21} + \tau_{20}} \quad (3.10)$$

$$\frac{dN_2}{dt} = N_2 - (g_2/g_1) N_1 \sigma_{21} c \phi + \frac{N_2}{\tau_{21}} - \frac{N_1}{\tau_{10}} \quad (3.11)$$

Here, the total atomic density is $N_{\text{tot}} = N_0 + N_1 + N_2$. In ideal four level laser, since τ_{10} can be set to $\tau_{10} \approx 0$, N_1 decreases for a short time from (3.11). Then, since $N_1 = 0$, inverted population is set to $N = N_2$. Therefore, the temporal change of the atomic density of level 2 is given by the following formula.

$$\frac{dN}{dt} = -N\sigma_{21}c\phi - \frac{N}{\tau_f} + W_p(N_{\text{tot}} - N) \quad (3.12)$$

Here, the fluorescence lifetime of a laser upper level is $1/\tau_f = 1/\tau_{21} + 1/\tau_{20}$. Moreover, excitation rate and excitation quantum efficiency are defined as $W_p = \eta_p W_{03}$ and $\eta_p = (1 + \tau_{32}/\tau_{31} + \tau_{32}/\tau_{30})^{-1}$, respectively.

Furthermore, the rate equation of the photon density of four level laser is given as follows.

$$\frac{d\phi}{dt} = N\sigma_{21}c\phi - \frac{\phi}{\tau_c} + \frac{fN}{\tau_f} \quad (3.13)$$

Here, ϕ , τ_c and f are the photon density, the lifetime of cavity and the rate that the photon generated by spontaneous emission is distributed to each mode of a cavity, respectively.

Saturation of gain

Next, the gain of the medium in the state where a strong photon field exists like a laser cavity is considered. By multiplying N by cross-section of stimulated emission, the gain coefficient to incident light intensity is given by the following formula.

$$\gamma(\nu) = \frac{\gamma_0}{1 + \frac{I}{I_s}} \quad (3.14)$$

Here, I_s is saturation light intensity. It is given $I_s = h\nu/\sigma_{21}\tau_f$ by applying approximation $W_p \ll 1/\tau_f$ to (3.12).

The condition of oscillation

The amplitude condition at the time of laser oscillating are generally expressed as follows.

$$r_1 r_2 \exp \gamma(\nu) - \alpha l = 1 \quad (3.15)$$

Here, r , l , $\gamma(\nu)$, α are reflectivity to an electrical field, cavity length, a gain coefficient and an absorption coefficient by loss, respectively. The round-trip gain in an oscillation threshold power is given as follows from (3.15). Subscript 1, 2 are shown mirror1 and mirror2 of a laser cavity.

$$2\gamma_{\text{th}}(\nu)l = 2\Delta N_{\text{th}}\sigma_{21}l = 2\alpha l - \ln R_1 R_2 \quad (3.16)$$

Here, R is reflectivity to light intensity ($R_i = |r_i|^2$). Moreover, generally, it can be set to $R_1 = 1$ and $-\ln R_2 = T$. Furthermore, if L_i is loss in a cavity, it can approximate $2\alpha l \approx L_i$.

Next, change of photon density is considered. After the initial value $\phi(0)$ goes and back to an optical cavity, it is decreased by $\phi(t) = \phi(0) \exp(-t/\tau_c)$ in time. Here, τ_c is a cavity life and is expressed as follows.

$$\tau_c = 2nl/c(2\alpha l - \ln R_1 R_2) \approx 2nl/c(L_i + T) \quad (3.17)$$

Moreover, a gain coefficient is expressed with the following formulas,

$$\gamma(\nu) = N_2 - (g_2/g_1)N_1\sigma_{21} \quad (3.18)$$

Therefore, the oscillation threshold power inverted population N_t is given by the following formula.

$$N_t = \frac{8\pi n^2 \nu^2 \tau_s}{c^2 g(\nu)} (\alpha - \ln R_1 R_2 / 2l) \approx (L_i + T) / 2\sigma_{21} l \quad (3.19)$$

Threshold and output power

Next, which $W_p N_{\text{tot}}$ is the atomic density generated by excitation at a laser upper level is considered. It is as follows to the excitation power I_{in} which entered into the laser medium.

$$W_p N_{\text{tot}} = \eta_p \eta_q \eta_a \eta_m I_{\text{in}} / h\nu_L V \quad (3.20)$$

Here, V is a volume of mode and η_q is excitation quantum efficiency, which is the rate that translates to a laser upper level among the numbers of atoms excited to the excited level is shown. Moreover, η_q is atomic quantum efficiency and is defined as $\eta_q = \nu_L / \nu_p$ which is a ratio of laser beam photon energy ν_L to an excitation photon energy ν_p . Furthermore η_a is excitation light absorption efficiency, and expresses with the rate that excitation light is absorbed by the laser medium. Then, η_m is mode matching efficiency, and shows the rate of the overlap of the oscillation region and the excitation region.

In the case of four level laser, unsaturated gain coefficient is obtained as follows by exceeding an oscillation threshold power in the range of $W_p \tau_f < 1$.

$$\gamma_0 = \sigma_{21} N_{\text{tot}} W_p \tau_f (W_p \tau_f + 1) \approx \eta_p \eta_q \eta_a \eta_m \sigma_{21} \tau_{\text{tau}} I_{\text{in}} / h\nu_L V \quad (3.21)$$

By substituting this value and saturation light intensity I_s for (3.14), a laser output is as follows.

$$I_o = \eta_c \eta_p \eta_q \eta_a \eta_{in} (I_{in} - I_{th}) \quad (3.22)$$

I_{th} is a laser threshold power, $\eta_c = T/(L_i + T)$ is coupling efficiency, and if A_{eff} is defined as the effective cross section of a laser beam, an oscillation threshold power is given by the following formula here.

$$I_{th} = \frac{h\nu_p A_{eff}}{2\eta_p \eta_a \sigma_{21} \tau_f} (L_i + T) \quad (3.23)$$

3.2.2 Laser oscillation power with placing plasma into a cavity

When plasma is placed into a cavity, the amplitude conditions for laser oscillation (3.15) are modified as follows.

$$r_1 r_2 \exp \gamma(\nu) - \alpha - \alpha_p l = 1 \quad (3.24)$$

Therefore, the gain is as follows,

$$2\gamma(\nu)l = 2\alpha l + 2\alpha_p l + \ln\left(\frac{1}{R_1 R_2}\right) \quad (3.25)$$

If T is loss in a cavity and L is the mirror loss, the total loss is

$$T + L + 2\alpha_p l \quad (3.26)$$

Since Cr:LiSAF laser is used in this research, in subsequent arguments, the formulas of threshold power and output power of Cr:LiSAF laser are used. They are described as follow,

$$I_{th} = \frac{\pi \omega_c^2 h \nu_p (T + L)}{2(\sigma_e - \sigma_{ESA}) \tau_f \eta} \quad (3.27)$$

$$I_o = \left\{ \left(\frac{h \nu_c}{h \nu_p} \right) \eta \left(\frac{\sigma_e - \sigma_{ESA}}{\sigma_e} \right) \left(\frac{T}{T + L} \right) \right\} (I_{in} - I_{th}) \quad (3.28)$$

Here, ω_c is mode radius of laser, ν_c is oscillating laser frequency, ν_p is pump laser frequency, σ_e is cross-section of stimulated emission, σ_e is cross-section of absorption of excited level and η is pump efficiency. Then, using (3.26), (3.27) and (3.28) are rewritten as follows,

$$I_{\text{th}} = \frac{\pi\omega_c^2 h\nu_p (T + L + 2\alpha_p l)}{2(\sigma_e - \sigma_{\text{ESA}})\tau_f \eta} \quad (3.29)$$

$$I_o = \left\{ \left(\frac{h\nu_c}{h\nu_p} \right) \eta \left(\frac{\sigma_e - \sigma_{\text{ESA}}}{\sigma_e} \right) \left(\frac{T}{T + L + 2\alpha_p l} \right) \right\} (I_{\text{in}} - I_{\text{th}}) \quad (3.30)$$

The absorbance in ICAS can be expressed as follows from these.

$$\left(\frac{\Delta I}{I_0} \right)_{\text{in}} = 1 - \frac{I_t(\text{output power with plasma})}{I_0(\text{output power without plasma})} = \frac{2\alpha_p l}{\alpha_0 + 2\alpha_p l} \frac{I_{\text{in}}}{I_{\text{in}} - I_{0\text{th}}} \quad (3.31)$$

Here, $\alpha_0 = T + L$, $I_{0\text{th}}$ is threshold power in case that there are no plasma into a cavity. Therefore, using (3.31), the absorbance obtained by ICAS is convertible for the absorbance in a single path.

3.3 Past results of intracavity laser absorption spectroscopy

In this section, past results research of intracavity absorption spectroscopy with a semiconductor laser are shown, and the points which should be improved are clarified. In the past research, in order to place an absorber into a laser cavity, an external cavity diode laser (ECDL) was developed. The applied external cavity is Littrow configuration. Littrow configuration forms the cavity between the high reflection facet of a semiconductor laser, and a diffraction grating. The detailed principle is shown in section 5.1.5. The absorber was placed between a semiconductor laser and a diffraction grating. The experiment system is shown below.

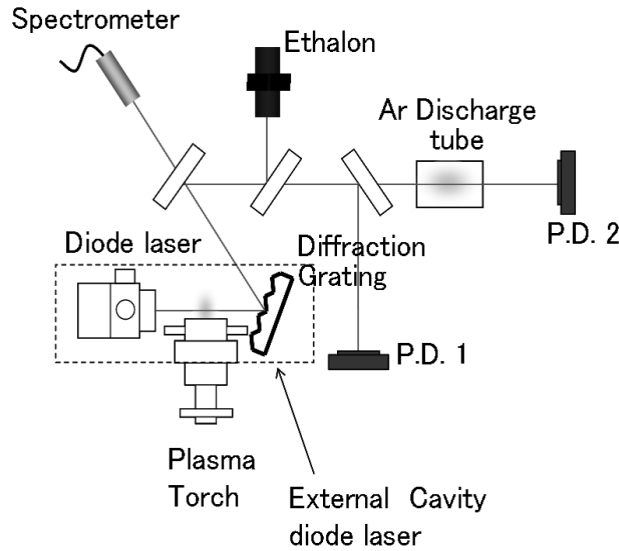


Figure 3.5: Schematic of intracavity absorption spectroscopy system with ECDL

The domain surrounded by the dotted line in Fig.3.5 is ECDL, and a plasma torch is placed as an absorber in it. Moreover, Ar discharge tube is a reference cell, and it is placed to obtain the reference signal for the absorption signal obtained by intracavity absorption spectroscopy. P.D.1 signal and P.D.2 signal which were obtained by this experiment are shown in the following graph. As being shown in Fig.3.6, the absorption signal was not obtained by P.D.1, or P.D.2. It is considered that the reasons are the unstable oscillation of ECDL by mode-hopping and internal loss of LD which was much larger than plasma loss. Here, mode-hopping is a sudden laser intensity variation caused at the time of the frequency modulation of laser. This is caused when the oscillation mode in a laser cavity changes. Then, the following two points are mentioned as an improving point.

- The solid state laser medium whose internal loss is generally smaller than a semiconductor laser is used.
- The system which suppresses mode-hopping and can sweep laser wavelength is developed.

The objectives of research was set up as shown in Section 1.4 based on these improving points.

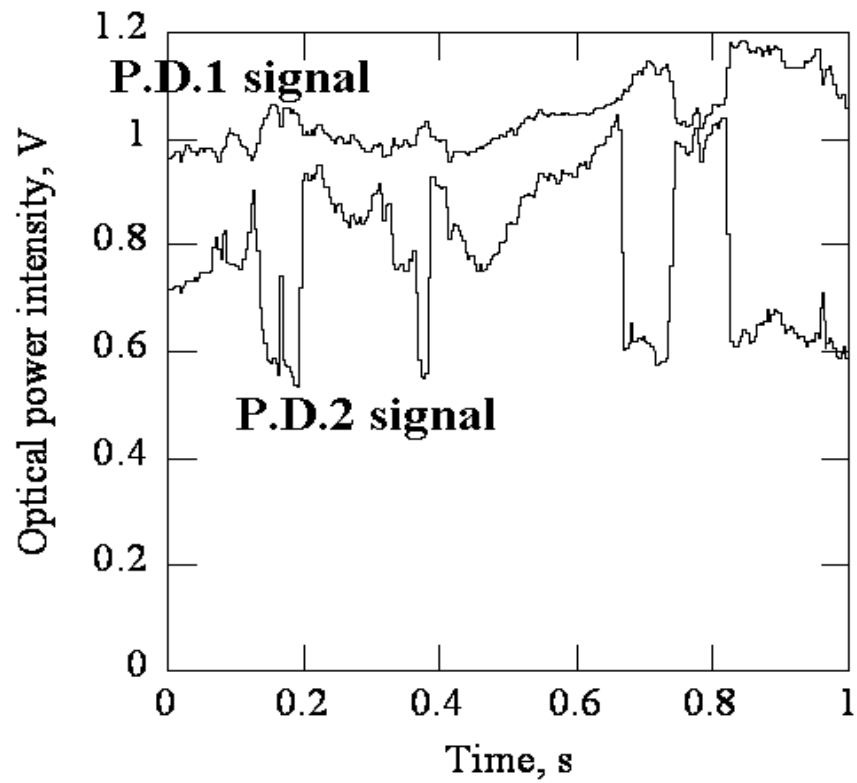


Figure 3.6: The results of intracavity absorption spectroscopy with ECDL

Chapter 4

Characteristics of Cr:LiSAF laser

In this chapter, characteristics of Cr:LiSAF used in this research is described.

4.1 Selection of a laser medium

There are two performances required of the laser used in this research. One is that the oscillation wavelength of laser is wide for measuring various objects. Another is that the laser system is a portable and compact system. Here, the solid-state laser mediums which has a wide oscillation wavelength range are shown in the following table.

Table 4.1: Laser mediums

Laser medium	Oscillation wavelength (nm)	Pump source
Ti ³⁺ :Al ₂ O ₃ (Ti:Sapphire)	660-1100	Argon laser
Cr ³⁺ :BeAl ₂ O ₃ (Alexandrite)	680-800	Xenon lamp
Cr ³⁺ :LiCaAlF ₆ (Cr:LiCAF)	750-900	laser diode
Cr ³⁺ :LiSrAlF ₆ (Cr:LiSAF)	700-1050	laser diode
Cr ⁴⁺ :Mg ₂ SiO ₄ (Forsterite)	1100-1300	Nd:YAG laser

This table shows that the laser system of Ti:Sapphire, Alexandrite or Forsterite becomes large and those portability becomes poor. On the other hand, Cr:LiCAF and Cr:LiSAF can be pumped by a laser diode, and those laser system becomes compact. In this research, Cr:LiSAF which has wide oscillation wavelength range among the two was chosen as the laser medium.

4.2 Cr:LiSAF

Against alexandrite laser, Cr:LiCAF [24] and Cr:LiSAF [25] which are chromium fluoride crystals were developed at the U.S. Livermore research institute in the 1980s. Especially Cr:LiSAF has spectral band width wider than Cr:LiCAF, and researches applied to all solid state wide band tunable laser, a ultrashort pulse laser, etc. have been carried out actively. This crystal is uniaxial nature and was first reported by S.A.Payne et al. of the U.S. Livermore research institute. Absorption and the emission spectrum of this crystal are shown in Fig.4.1.

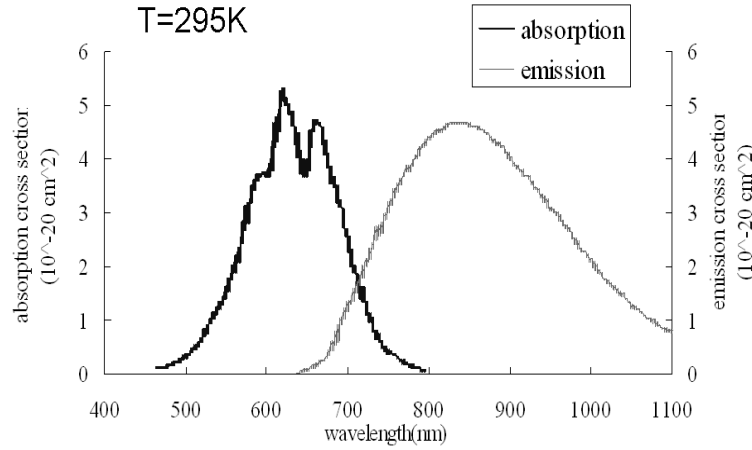


Figure 4.1: Absorption and the emission spectrum of Cr:LiSAF

Cr^{3+} exists in low field site. The energy difference of 4T_2 and 2E is $\Delta < 0$, and negative value. For this reason, 2E level entered into 4T_2 level like the energy level of Fig.4.2. The transition of ${}^4T_2 \rightarrow {}^4T_1$ is ESA (excited state absorption) and worsens the characteristic of laser. However, as for the feature, there are few these effects at this LiSAF crystal. Cr:LiSAF is suitable for the laser for high energy accumulation by the flash lamp excitation since its fluorescence lifetime is a long time. Although BeAl_2O_4 of an alexandrite crystal is much better than LiSAF in respect of heat conduction and hardness, it is hard to glow a crystal several millimeters or more in diameter. Moreover, Be must be treated, it is toxic and treatment is troublesome. However, LiSAF has advantages in respect of growth being easy, and growth of the large-sized crystal with which a diameter amounts to several centimeters being possible, and being able

to add Cr so much etc. Therefore, Cr:LiSAF is used for amplification of ultrashort pulse laser, an oscillation with an InGaAlP system laser diode (wavelength 670 nm band) is possible, and the use as all the solid state laser is also started.

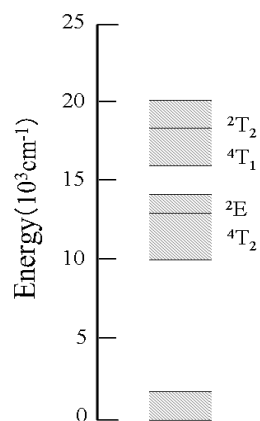


Figure 4.2: Energy level of transition metal ion

4.3 Tuning characteristics of Cr:LiSAF

As the foregoing section described, Cr:LiSAF has a wide emission spectrum. Therefore, the expectation as a tunable laser is also high, and research has been performed actively. In this section, the previous researches by other research groups are introduced and the subject and solution at the time of treating Cr:LiSAF laser as a tunable laser are described .

Because the emission cross-section-and-lifetime product of Cr:LiSAF is approximately 50 times smaller than that of Nd:YAG, it is difficult to obtain a high gain, especially in the diode-pumped configuration owing to the extent of the emitter in the diode array. Then, the output and tuning characteristics of a Cr:LiSAF laser are very sensitive to an optical loss in the cavity. The tuning bandwidth of the Cr:LiSAF lasers including dispersion elements (i.e., birefringent filter, diffraction grating etc.) in the main cavity has been limited to $\sim 100\text{nm}$ owing to the insertion loss. Especially in the longer wavelength region over 900nm , it is difficult to maintain the oscillation due to the lower emission cross section. The examples of reports are shown in Table 4.1.

Table 4.2: The examples of tuning Cr:LiSAF laser

Authors	Tuning method	Tuning width	Reference
Falcoz <i>et al.</i>	The Lyot filter	120nm	[26]
Zenzie <i>et al.</i>	Birefringent filter plates	50nm(from 810 to 860nm)	[27]
Zawischa <i>et al.</i>	Birefringent filter plates	78nm(from 814 to 892nm)	[28]

The coupled cavity configuration is useful for the tuning of such low-gain laser materials, because the tuning elements with high optical insertion loss can be separated by the coupling mirror from the low-loss main cavity including the laser medium and the effect of the loss in the tuning characteristics. The coupled cavity consists of two cavities whose length are L_1 and L_2 which are combined with the common reflection mirror as shown in Fig.4.3. When these two cavities resonate simultaneously, the laser oscillates.

When two cavities are not coupled, resonance frequency is $mc/2L_1$ and $m'c/2L_2$, respectively. Here, m and m' are integer. Moreover, the resonant wavelength gaps at this time are $\lambda^2/2L_1$ and $\lambda^2/2L_2$, respectively (Fig4.4).

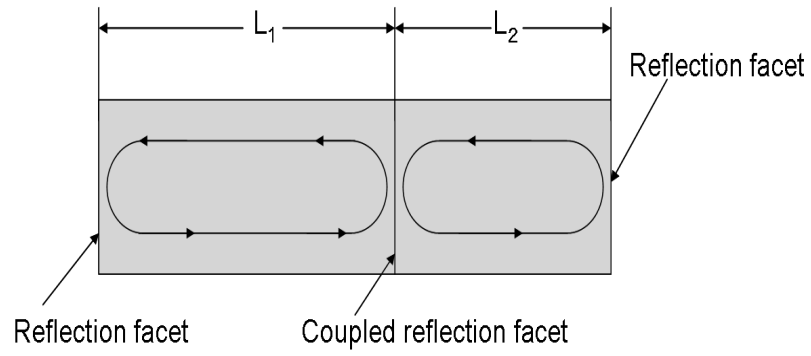


Figure 4.3: Schematic of a coupled cavity

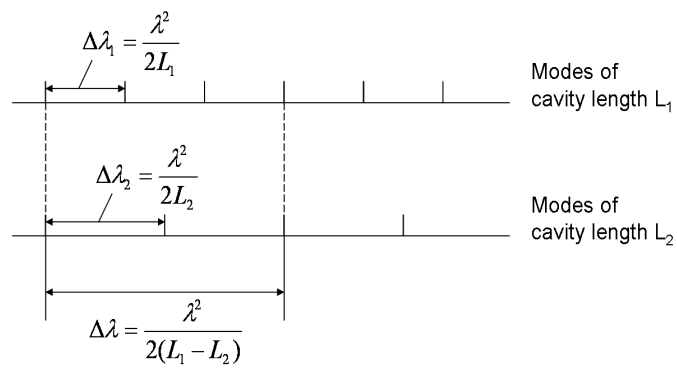


Figure 4.4: The resonance mode of a coupled cavity

$$\Delta\lambda = \frac{\lambda^2}{2(L_1 - L_2)} \quad (4.1)$$

When two cavities resonate simultaneously, the resonant wavelength gap $\Delta\lambda$ is as (4.1). This shows that mode gap becomes very large compared with the case of one cavity. Therefore, the oscillation by single longitudinal mode also becomes easy. The example using a coupled cavity is shown in Table 4.2.

Table 4.3: The examples of Cr:LiSAF laser with a coupled cavity

Authors	Coupled type	Tuning width	Reference
Q.Zhang <i>et al.</i>	FP cavity and three Lyot filters	85nm (from 850 to 935nm)	[29]
N.J.Vasa <i>et al.</i>	FP cavity and optical fiber grating	$\sim 0.5\text{nm}$	[30]
M.Ihara <i>et al.</i>	FP cavity and a diffraction grating	148nm (from 814 to 962nm)	[31]
Y.Nagumo <i>et al.</i>	a ring cavity and the ring cavity with a diffraction grating	136nm (from 800 to 936nm)	[32]

Thus, the tunable range over 100nm can be obtained by using a coupled cavity. However, it is considered that the tuning operation is not a continuous sweep but a sweep with mode hop. In order to perform mode hop free tuning, it is necessary to modulate two cavity length synchronously.

Chapter 5

Experimental results and Discussion

In this chapter, results of characteristics of developed Cr:LiSAF laser and intracavity absorption spectroscopy with the laser are shown and discussed.

5.1 Characteristics of Cr:LiSAF Laser (25mm cavity)

In order to perform the intracavity absorption spectroscopy, a laser cavity length have to be become long. However, since a cavity loss in the long laser cavity become large, it was considered that the oscillation of the Cr:LiSAF laser with a long cavity was difficult to operate from the start. Therefore, the oscillation experiment in the cavity length of 25mm was performed as first step, and an oscillation spectrum, output power, and a beam pattern was measured. Moreover, Littman configuration as an external cavity was coupled to this laser cavity, and the experiment of selecting wavelength was performed. In this section, the results are shown and discussed.

5.1.1 Experimental system

The schematic of a laser experiment system with 25 mm-cavity is shown in Fig.5.1. Furthermore, the outline of the experimental device for every component is shown below.

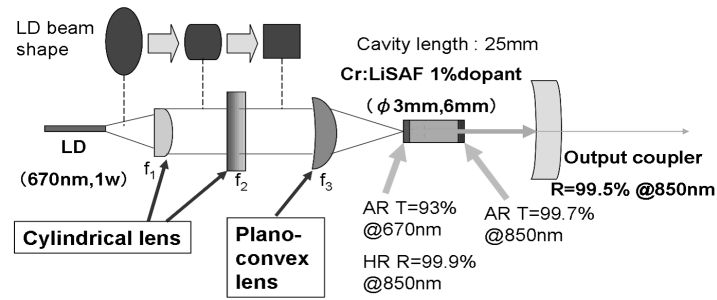


Figure 5.1: Schematic of Cr:LiSAF laser system with a 25mm-cavity

Laser diode

In this system, the laser diode (HPD1310, HPD.inc) was used as a pump source. Wavelength and maximum output power of this laser diode are 670nm and 1W at 1600mA. Moreover, as a driver system of this laser diode, LD driver with a built-in temperature controller and LD attachment-and-detachment head (Asahi data systems.inc) was used. Since it can connect with LD drive system easily, without soldering can package type LD, a risk of breaking LD can be avoid by LD head. A continuous oscillation is possible, the temperature control function incorporating a Peltier device and a thermistor is included in the inside of a head, and the temperature of LD can be adjusted. Since used LD is high power LD, its heat value is also larger than the heat value of general LD. Therefore, in this research, LD head (ALTH-103AC) which includes the Peltier device (2A and 5.6V) was used, a heat sink was attached to the head bottom, and air cooling was carried out by a small fan from an outside as a measure against heat. Furthermore, when the surge protection circuit is contained in a LD head, in order to exceed the limit voltage of LD driving device, the limiter worked and sufficient LD current was not supplied. Therefore, the surge protection circuit is not contained in this LD head. Then, the protect cage of the punching metal was attached to the circumference of the head and the connector of acrylics was used for connection with a pole as a measure against surge, and LD was insulated to the surge which incomes from an optical bench or the outside to it. The LD driver (ALP-7233CA) which can injects a maximum current of 2A was used as LD driver with a built-in temperature controller. The LD part is shown in Fig.5.2.

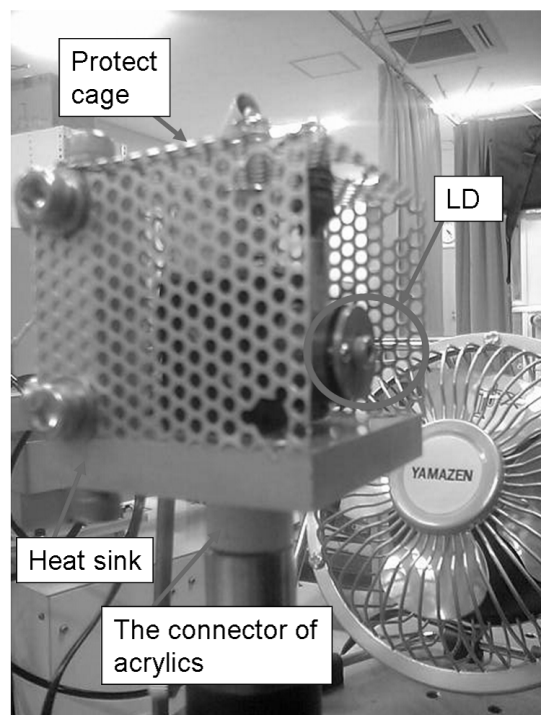


Figure 5.2: Picture of pump LD laser system

Lenses

Two cylindrical lenses and one plano-convex lens were used as focusing optics. Since the beam pattern of LD is the elliptical shape, in order to raise focusing density, it is necessary to rectify it circularly. Therefore, the cylindrical lens ($f=12.7\text{mm}$:LJ1805L1-B and 60.0mm :LJ1430L1-B THORLABS.inc) rectified the perpendicular axial component and level axial component of LD beam, respectively. In order to suppress spherical aberration by a lens, an plano-convex lens ($f=25.4\text{mm}$:LSB01 THORLABS.inc) was used as a focusing lens. Thereby, the diameter of focusing spot was set to $120\times 100\text{ }(\mu\text{m}^2)$.

Cr:LiSAF crystal

Cr:LiSAF crystal in this research is made by CASTECH.inc. The size of this crystal is 3mm in diameter and 6mm in length. Then, this is doped 1% Cr ion. One side of the crystal has a high reflection coating ($R=99.9\%$) at 850nm and an anti-reflection coating ($T=93.0\%$) at 670nm, and the other side has an anti-reflection coating ($T=99.7\%$) at 850nm. In order to promote heat radiation of this crystal, the crystal was held with the holder made from aluminum. The photograph of the crystal is shown in Fig.5.3.

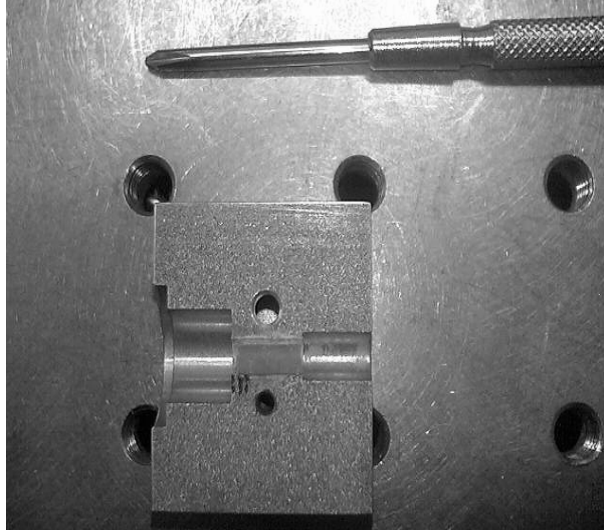


Figure 5.3: Picture of Cr:LiSAF crystal

Output coupler

The output coupler (CVI.inc) which is 1inch in diameter was used as a cavity mirror. The output coupler has a high reflection coating ($R=99.5\%$) at 850nm and its curvature radius is 50mm.

Long pass filter

When the laser beam is detected, LD emission which is a pump source is also detected simultaneously. Therefore, LD emission was cut by the long pass filter. A long pass filter is laminated 1/4 wave plate, and it uses not absorption but interference in order to separate the spectrum range. The long pass filter (FEL0700 THORLABS.inc) cuts off emission below 700nm in wavelength. The transmittance is larger than 80% in the region of wavelength is longer than 700nm, and 0.01% in the region of wavelength is shorter than 700nm.

Spectrometer

As detection device of a laser beam, the spectrometer (EPP2000C-SR StellarNet.inc) was used. The spectrometer has a 2048 element CCD detector. The optical input is via fiber optic cable with SMA-905 termination. The instrument is designed to be vibration tolerant with no moving parts or detector sockets, suitable for portable. The instrument connects directly to a PC's USB port. The detectable region is from 200nm to 1080nm and the wavelength resolution is $\sim 0.5\text{nm}$.

5.1.2 Output spectrum

The spectrum of developed Cr:LiSAF laser is shown in Fig.5.4.

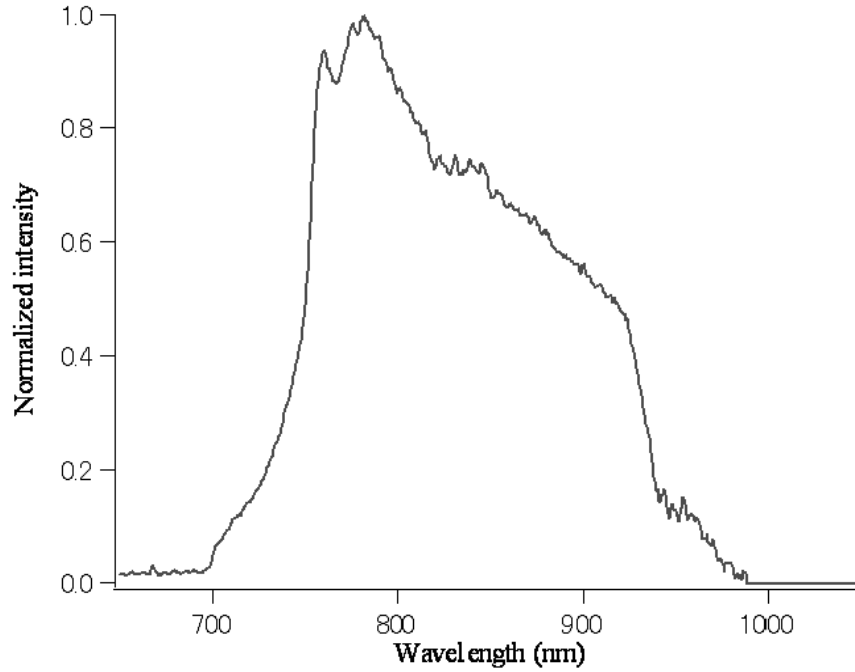


Figure 5.4: The spectrum of Cr:LiSAF laser (25mm cavity)

As shown in this figure, a broad emission wavelength which is from 750 to 950 nm was observed. Although it seems that this profile is continuous, the reason is that the spectrometer does not have enough wavelength resolution. Since the laser cavity in this system is the Fabry Perot cavity, it is considered that the spectrum includes many longitudinal modes in fact. Since the laser cavity is 25mm, free spectral range (FSR) is estimated to be 6GHz ($\sim 0.01\text{nm}$) from a formula (2.30).

5.1.3 Beam pattern

Next, the beam pattern of Cr:LiSAF laser is shown in Fig.5.5 and Fig.5.6.

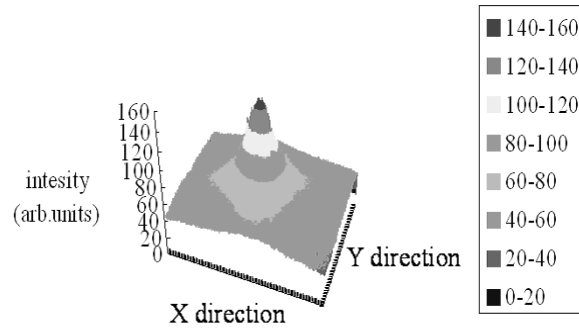


Figure 5.5: The spatial distribution of Cr:LiSAF laser beam

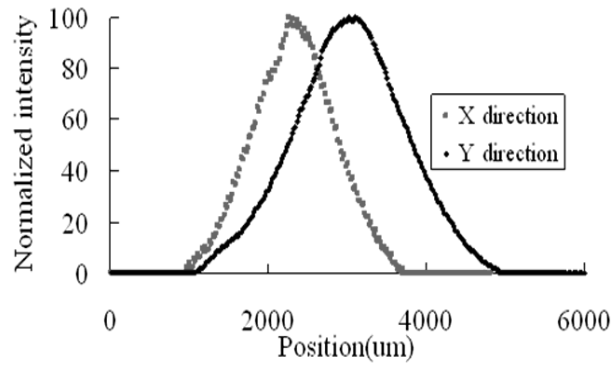


Figure 5.6: The profile of Cr:LiSAF laser beam

From this result, this laser beam is considered that a beam diameter is about 2500 μm and single transverse mode.

5.1.4 Laser output power

In this section, a characteristic of laser output is described. The relationship of pump power and Cr:LiSAF laser output power is shown in Fig.5.7.

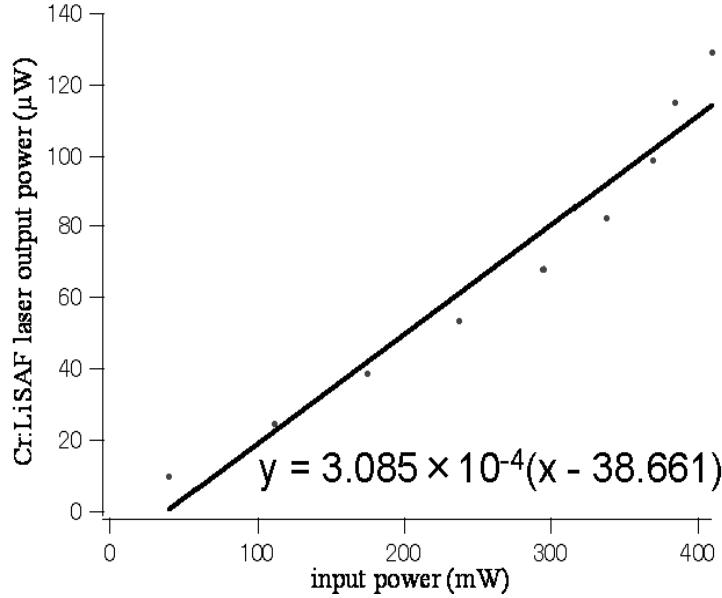


Figure 5.7: The relationship of pump power and Cr:LiSAF laser output power (25mm cavity)

The points in this graph show the relationship of input and output power, and the straight line is the fitting line of them. The formula in this graph expresses the straight line. It is found from this graph that the maximum output power of Cr:LiSAF laser is $129 \mu\text{W}$. Moreover, the oscillation threshold power and slope efficiency were calculated with 38.6mW and 0.03% from the formula obtained by fitting. The output power is weak. However, if a photo-multiplier is used, the absorbance can measure enough. Moreover, although it was observed that the Doppler width becomes broad with increasing of laser intensity because of absorption saturation [33], it is considered that the problem of broadening the Doppler width is avoidable by this laser.

5.1.5 Selecting laser wavelength

With this laser system, selecting laser wavelength was experimented. As described in chapter4, the laser cavity has to be changed into a coupled cavity because the characteristic of selecting wavelength of a Cr:LiSAF laser is very sensitive to an optical loss in the cavity. In this research, in order to avoid complication of the laser system, Littrow configuration [34], which is easy to construct, as an external cavity was adopted and the experiment was performed.

A diffraction grating is used in Littrow configuration. The first order light dispersed by the grating is return to the laser medium. As the result, a cavity is formed between high refraction coating of the laser element and a diffraction grating. Then, since an angle of incidence and the angle of diffraction become equal, a diffraction condition becomes like the following formula.

$$\lambda = 2d \sin \theta_i \quad (5.1)$$

Moreover, in order to oscillate the laser, it is required for the cavity length L_{ext} to become an integral multiple of the half-wave length of the laser. Therefore, the resonance condition expressed with the following formula are fulfilled.

$$L_{\text{ext}} = m \frac{\lambda}{2} \quad (5.2)$$

As mentioned above, the laser is oscillated when (5.1),(5.2) are realized simultaneously in Littrow configuration.

In this system, since the laser cavity is coupled cavity, it has become instead of high refraction coating of the output coupler being one of laser medium mentioned above. Therefore, the auxiliary cavity is formed between high refraction coating of the output coupler and a diffraction grating, and the cavity length is 330mm for arrangement of other optical devices. The grating in this system has 830 grooves/mm, brazed wavelength 800nm (43849-H Edmund Optics japan.inc). The laser output was detected by the spectrometer (StellarNet.inc). The laser system and the result of experiment is shown in Fig.5.8 and Fig.5.9.

It is found that wavelength could be selected from 828nm to 910.5nm. This selecting range was much wider than the selecting wavelength region of general laser diodes, and the result which shows the advantage of this laser was obtained. However, minimum full width half maximum (FWHM) of beam profile was 2.3nm. Therefore, it is considered the beam profile was not single longitudinal mode. The reason is considered that the wavelength dispersion by a grating was not enough. From Rayleigh criterion [35], the wavelength resolution of a grating is expressed as follows,

$$\frac{\lambda}{\Delta\lambda} = m \times N \times W \quad (5.3)$$

Here, λ , $\Delta\lambda$, m , N and W are wavelength, wavelength resolution, order of diffraction, grooves of grating and beam diameter, respectively. In this case, since $\lambda=850(\text{nm})$, $m=1$, $N=830(\text{grooves/mm})$, $W=2.5(\text{mm})$, the resolution $\Delta\lambda$ is 0.4nm . However, When a diffraction grating actually is used together with other optical elements, a spectral line is spread further by the imperfection or aberration of other optical elements (a lens, a mirror, etc.), or the size of a light source or a slit. For this reason, since the dispersible wavelength difference $\Delta\lambda$ of the spectrum becomes large, it is considered that the resolution in the whole optical system is getting worse than the estimated resolution of the diffraction grating. Therefore, it is considered that FWHM of the selected wavelength became 2.3nm . From this discussion, and it is considered that wavelength selection in thinner line width can be performed by a diffraction grating with more grooves is used and extending a beam diameter. Then, it is considered that mode-hop was occurred with selecting wavelength because only the grating angle was moved. For mode-hop free tuning, an output coupler of main cavity is needed to move simultaneously with adjusting the grating angle.

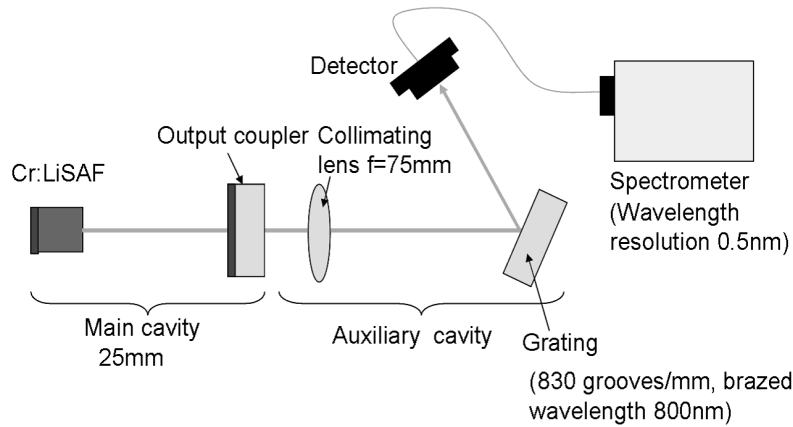


Figure 5.8: Schematic of the laser system for selecting wavelength

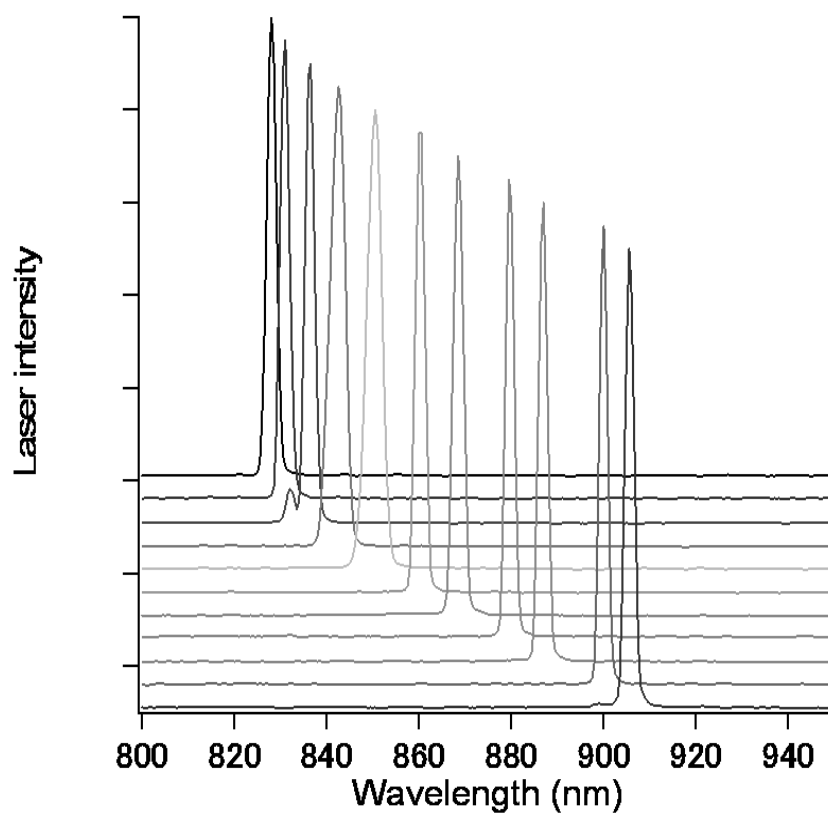


Figure 5.9: The result of selecting wavelength

5.2 ICAS measurement with Cr:LiSAF laser (150mm cavity)

Since the oscillation of Cr:LiSAF laser was observed, in order to perform ICAS measurement which is the objective of this research, the laser system was changed into the system which set the cavity length to 150mm. Although, construction of the experiment system is the same as Fig.5.1, the radius of curvature of output coupler is changed into 300mm, and the high reflection coating at 840nm center is coated on its facet in order to change the cavity length into 150mm.

5.2.1 Characteristics of Cr:LiSAF laser (150mm cavity)

The laser spectrum and the relationship of inputpower and outputpower are shown in Fig.5.10 and Fig.5.11. The broad range of from 750 to 950nm was observed like the time of the 25mm cavity from the results. Then, the maximum output power, the oscillation threshold power and slope efficiency were 12.8 μ W, 42.4mW and 0.003%, respectively.

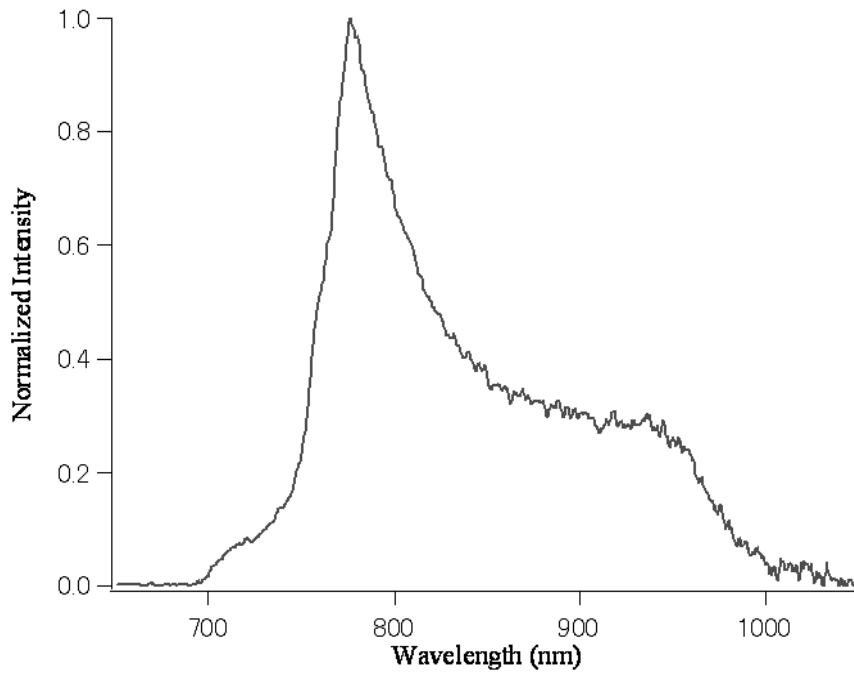


Figure 5.10: The spectrum of Cr:LiSAF laser (150mm cavity)

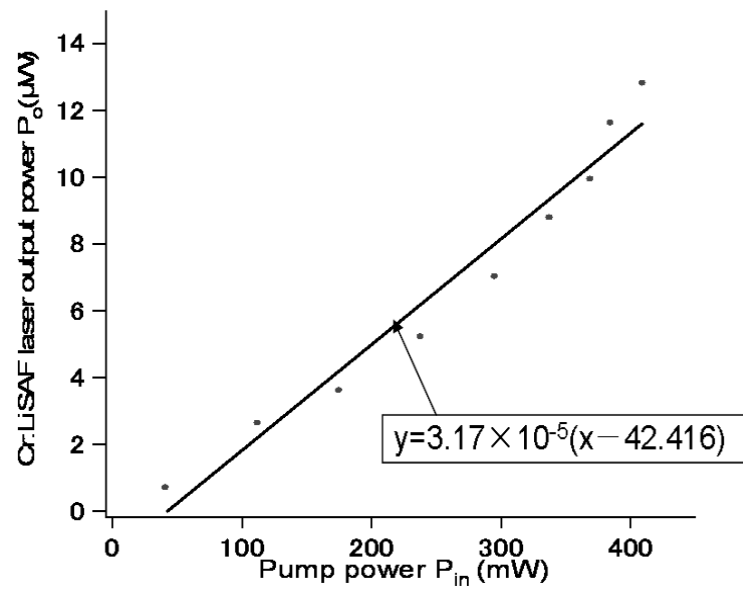


Figure 5.11: The relationship of pump power and Cr:LiSAF laser output power (150mm cavity)

5.2.2 The magnification of absorbance in ICAS

From the obtained result, the magnification of the absorbance in ICAS can be estimated. From (3.29) and (3.30), the cavity internal loss was estimated as shown in Table 5.1.

Table 5.1: Parameters for estimation

MeasuredParameters		Fitting Parameters	
P_{th0}	Slope efficiency	T+L	T/(T+L)
42.4mA	0.003%	0.0052	0.00007

From these parameters and formula, the magnification of the absorbance in the case of placing a sample absorber in the laser cavity was estimated. The result is shown in Fig.5.12.

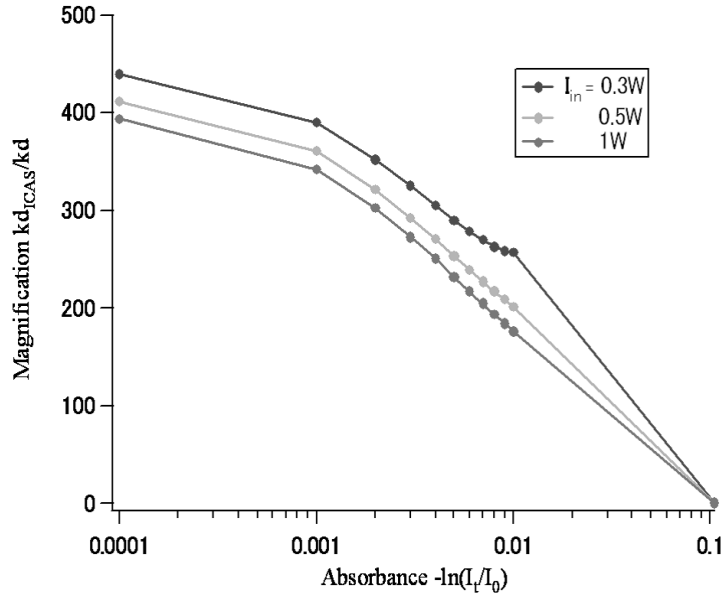


Figure 5.12: The magnification of absorbance

The magnification was estimated in the range of absorbance which is from 0.1 to 0.0001. kd_{ICAS} and kd_{LAS} on vertical axis are the absorbance in ICAS and in LAS, respectively. From these results, it is found that the higher input power approaches to the threshold power, the more the magnification of absorbance gets. At the region where absorbance is less than 0.1, it is found that absorbance in ICAS was expected about hundreds of times larger than that in LAS.

5.2.3 The measurement of absorbance in ICAS

With the Cr:LiSAF laser, the plasma absorbance in ICAS was measured and compared with the absorbance in LAS. The measurement system is shown in Fig.5.13 and Fig.5.14.

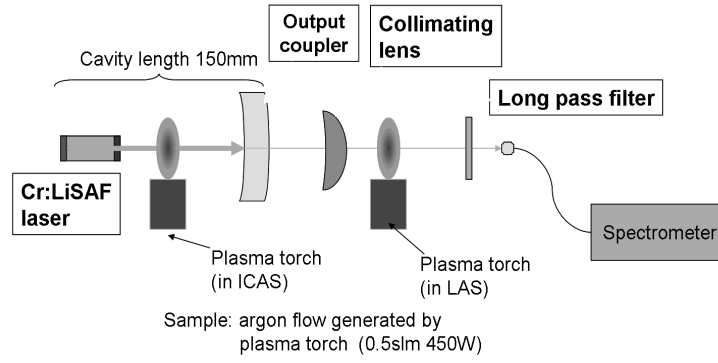


Figure 5.13: Schematic of the measurement system

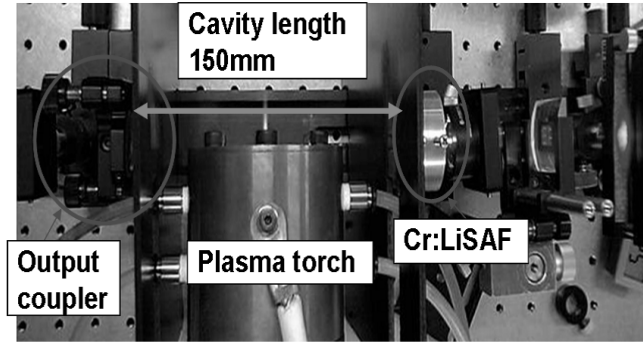


Figure 5.14: Picture of the measurement system

The laser beam is collimated by $f=200\text{mm}$ plano-convex lens (THORLABS.inc) and its diameter is about $2500\mu\text{m}$. The laser spectrum was measured by the spectrometer. An argon flow generated by plasma torch was used as a test sample. The mass flow rate and input power were 0.5slm and 450W, respectively. The input power of the laser was 384mW. In this measurement, since the line width of the beam by selecting wavelength was not thin enough, measurement was performed without selecting wavelength. The absorbance was estimated from the change of laser spectrum with and without an absorption of argon. The results of the absorbance in ICAS and LAS are shown in Fig.5.15.

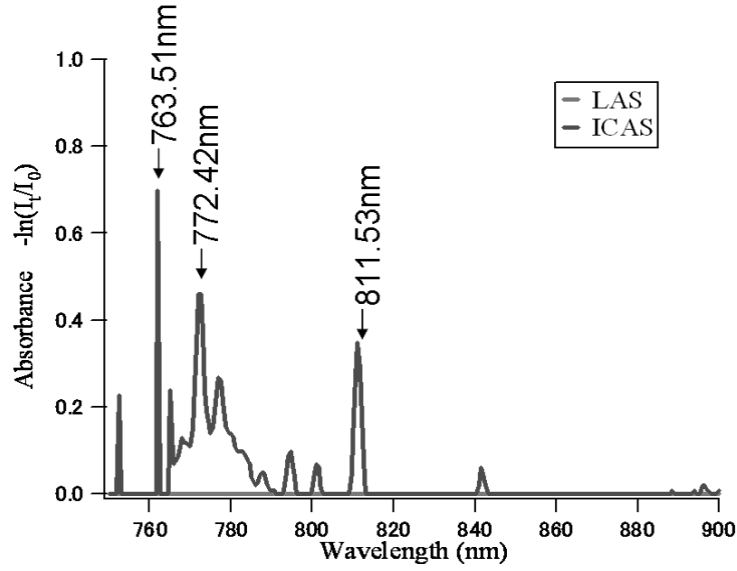


Figure 5.15: The absorbances in ICAS and LAS

The absorbance in ICAS and LAS was shown in Fig.5.15. While the absorption line of Ar was detected clearly in ICAS, it was not detected at all in LAS. This shows that absorption sensitivity is enhanced by ICAS qualitatively. Moreover, to absorption of five absorption lines of argon which have appeared strongly, the absorbance in the single path was estimated the magnification by using (3.31). The result is shown in Table 5.2.

Table 5.2: The magnification of absorbance

Wavelength (nm)	763.51	772.42	811.53
The absorbance of multi path kd_{ICAS}	7.02×10^{-1}	4.62×10^{-1}	3.47×10^{-1}
The absorbance of single path kd_{LAS}	4.33×10^{-3}	1.82×10^{-3}	1.16×10^{-3}
Mgnification $kd_{\text{ICAS}}/kd_{\text{LAS}}$ (from the expeliment)	161.7	253.7	297.8

From these results, it is found that the magnification of absorbance is about 200times ,and the magnification obtained from the experiment and that obtained from 5.2.2 are mostly in agreement. Then, number density of meta-stable argon is estimated using the absorbance obtained by this system. The relation be-

tween an integrated absorption coefficient and number density is expressed like (2.21). The parameter of each absorption line is as follows.

Table 5.3: The parameter of absorption lines

Wavelength (nm)	763.51	772.42	811.53
g_j	5	3	7
g_i	5	1	5
A_{ji}	2.45×10^7	1.17×10^7	3.31×10^7

Moreover, at the time of calculation, absorption length and absorption line width were assumed to be 0.002m and 10GHz, respectively. As a result, number density of meta-stable argon was obtained as follows.

Table 5.4: Number density of meta-stable argon

Wavelength (nm)	763.51	772.42	811.53
Number density (m^{-3})	3.8×10^{16}	9.8×10^{16}	9.4×10^{15}

It is considered that every number density of meta-stable argon is $10^{15} \sim 10^{16}$ from these results. The order of these values are comparable as the result obtained by experiment with the plasma torch in the past [36]. It was proved that the absorption spectroscopy using this system is effective from this.

Chapter 6

Conclusion

1. In order to observe an oscillation of Cr:LiSAF laser, it experimented with 25mm cavity, and oscillation in multi longitudinal modes was observed. The laser wavelength was 750-950nm, maximum power was $129\mu\text{W}$, threshold power was 38.6mW and slope efficiency was 0.03%.
2. A coupled cavity with Littrow configuration was constructed. Laser wavelength was selected 828-910.5nm and minimum FWHM is 2.3nm in 25mm cavity.
3. Cr:LiSAF laser with long cavity was constructed for ICAS. The laser oscillated 750-950nm (Maximum power $12.8\mu\text{W}$, threshold 42.4mW, slope efficiency 0.003%) in 150mm cavity.
4. In the case of ICAS with this laser (150mm cavity), maximum magnification of absorbance was estimated hundreds of times.
5. The absorption signal in ICAS and LAS of argon flow were detected with developed Cr:LiSAF laser. It was estimated that the magnification was about 200 times and the number density of meta-stable argon was about $10^{16}(\text{m}^{-3})$.

Reference

- [1] Bertin, J. J., " Hypersonic Aerothermodynamics, " AIAA Education Series, AIAA, Inc., Washington, DC (1994)
- [2] Throckmorton, D. A., "Shuttle Entry Aerothermodynamic Flight Research: The Orbiter Experiments Program, " Journal of Spacecraft and Rockets, Vol. 30, No. 4, 1993, pp. 449-465.
- [3] Inatani, Y., Hasegawa, S., and Komatsu, T., " Present Status of Arc Heated Facilities in the World and the Future Plan, " Proceedings of the 26th Symposium on Fluid Mechanics, 1994, pp. 101-104
- [4] Ito, T., Ishida, K., Mizuno, M., Sumi, T., Fujita, K., Nagai, J., Murata, H., and Matsuzaki, T., " Heating Tests of TPS samples in 110kW ICP-heated wind tunnel, " ISTS 2004-e-20, (2004)
- [5] Yamada, T., and Inatani, Y., " Inductively-coupled High Enthalpy Flow Generator for Planetary Entry Probes, " ISTS 2004-e-21 (2004)
- [6] Smith, R. K., Wagner, D. A., and Cunningham, J. W., " A Survey of Current and Future Plasma Arc-heated Test Facilities for Aerospace and Commercial Applications, " AIAA Paper 98-0146, Jan. (1998)
- [7] Auweter-Kurtz, M., " Diagnostic Tools for Plasma Wind Tunnels and Reentry Vehicles at the IRS, " Measurement Techniques for High Enthalpy and Plasma Flows, NATO Research and Technology Organization Proceedings RTO-EN-8, Neuilly-Sur-Seine Cedex, France, 2000, pp. 2B-1-2B-78
- [8] Sharma, S. P., Park, C., Scott, C. D., Arepalli, S., and Taunk, J., " Arcjet Flow Characterization, " AIAA Paper 96-0612, (1996)
- [9] Winovich, W., " On the Equilibrium Sonic-Flow Method for Evaluating Electric-Arc Air-Heater Performance, " NASA TN D-2132, 1964

- [10] Fletcher, D. G., " Measurement Requirements for Improved Modeling of Arcjet Facility Flows, " Measurement Techniques for High Enthalpy and Plasma Flows, NATO Research and Technology Organization Proceedings RTO-EN-8, Neuilly-Sur-Seine Cedex, France, 2000, pp. 3A-1-3A-27.
- [11] Schoenemann, A. and Auweter-Kurtz, M., " Mass Spectrometric Investigation of High Enthalpy Plasma Flows, " Journal of Thermophysics and Heat Transfer, Vol. 9, No. 4, 1995, pp. 620-628
- [12] W. Demtroder, " Laser Spectroscopy, " second edition, Berlin, Springer Verlag, 1996
- [13] Demtroder, W., " Laser Spectroscopy, " second ed., Berlin, Springer Verlag, 1996.
- [14] NIST Atomic Spectra Database, [http : //physics.nist.gov/cgi – bin/AtData/main_asd](http://physics.nist.gov/cgi-bin/AtData/main_asd)
- [15] M.Matsui, 2005 Master thesis, the university of tokyo.
- [16] Matsui, M., Komurasaki, K., and Arakawa, Y., " Laser Diagnostics of Atomic Oxygen in Arc-Heater Plumes ", 40th AIAA Aerospace Science Meeting and Exhibit, AIAA 02-0793
- [17] Matsui, M., Takayanagi, H., Oda, Y., Komurasaki, K., Arakawa, Y., " Performance of arcjet-type atomic-oxygen generator by laser absorption spectroscopy and CFD analysis ", Vacuum, Vol.73(3-4), pp.341-346 (2004)
- [18] Matsui, M., Hedrich, G., Komurasaki, K. and Auweter-Kurtz, M., " Laser Absorption Spectroscopy in Inductive Plasma Generator Flows ", 42nd AIAA Aerospace Sciences Meeting and Exhibit, AIAA 04-1222, 2004, Reno
- [19] H.Edner, P.Ragnarson, S.Spannare, S.Svanberg "Differential optical absorption spectroscopy (DOAS) system for urban atmospheric pollution monitoring" Appl.Opt. Vol.32 1993 pp.327
- [20] J.Ballard, K.Strong, J.J.Remedios, M.Page, W.B.Johnston "A coolable long path absorption cell for laboratory spectroscopic studies of gases" J.Quant.Spectrosc. Radiat. Transfer Vol.52 1994 pp.677-691
- [21] Anthony O'Keefe and David A. G. Deacon, " Cavity ring-down optical spectrometer for absorption measurements using pulsed laser sources, " Review of scientific Instrument, Vol.59(12), pp.2544-2551 (1982)
- [22] O'Keefe,A., "Integrated cavity output analysis of ultra-weak absorption" Chemical Physics Letters, Vol.293, pp.331-336,(1998)

- [23] V. M. Baev, T. Latz, P. E. Toschek, " Laser intracavity absorption spectroscopy ", Applied Physics B: Lasers and Optics, Vol. 69, pp171-202 (1999)
- [24] S.A.Payne, L.L.Chase, H.W.Newkirk, L.K.Smith and W.F.Krupke, " LiCaAlF₆:Cr³⁺: A promising new solid-state laser material" IEEE J.Quant. Electron., 24, 2243 (1988)
- [25] S.A.Payne, L.L.Chase, L.K.Smith, W.F.Krupke and H.W.Newkirk," Laser performance of LiSrAlF₆:Cr³⁺" J.Appl.Phys., 66, 1051 (1989)
- [26] F.Falcoz, F.Balembois, P.Gerges, and A.Brun, "All-solid-state continuous-wave tunable blue-light source by intracavity doubling of a diode-pumped Cr:LiSAF laser," Opt.Lett., vol.20, no.11,pp.1274-1276,1995
- [27] H.H.Zenzie, A.Finch, and P.F.Moulton, "Diode-pumped, single-frequency Cr:LiSAF6 ring laser," Opt.Lett., vol.20, no.21,pp.2207-2209,1995
- [28] I.Zawischa and A.I.Ferguson, "Diode-pumped, continuous-wave, single-mode, tunable Cr:LiSAF6 ring laser," Opt.Lett., vol.21, no.1,pp.45-47,1996
- [29] Q.Zhang, G.J.Dixon, B.H.T.Chai, and P.N.Kean, "Electrically tuned diode-laser-pumped Cr:LiSAF6 laser," Opt.Lett., vol.17, no.1,pp.43-45,1992
- [30] N.J.Vasa, T.Okada, M.Maeda, T.Mizunami, and O.Uchino, "Single-mode cw Cr³⁺:LiSAF6 laser using an external fiber grating," Opt.Lett., vol.21, no.18,pp.1472-1474,1996
- [31] M.Tsunekane, M.Ihara, N.Taguchi and H.Inaba, "Analysis and design of widely tunable diode-pumped Cr:LiSAF lasers with external grating feedback," IEEE J.Quantum.Electronics, Vol.34, no.7 pp.1288-1296, 1998
- [32] Y.Nagumo, N.Taguchi and H.Inaba, "Widely tunable continuous-wave Cr³⁺:LiSrAlF₆ ring laser from 800 to 936 nm," Appl.Opt, Vol.37, no.21, pp.4929-4932 1998
- [33] M.matsui, K.Komurasaki, S.Ogawa and Y.Arakawa, "Influence of laser intensity on absorption line broadning in laser absorption spectroscopy" , Journal of applied physics. 100 (2006) 6.
- [34] R. Ludeke and E. P. Harris, " Tunable GaAs Laser in an External Dispersive Cavity, " Applied Physics Letters, Vol. 20, pp.499-500 (1972)
- [35] M.ooi," 光学素子の基礎と活用法 " 学会出版センター p.p.126

- [36] H.Takayanagi, M.Matsui, K.Komurasaki, H.Ochimizu , Y.Arakawa,"Diagnostics of plasma torch flow by Cavity Enhanced Absorption Spectroscopy", Journal of the Japan Society for Aeronautical and Space Sciences, Vol.55, Issue 642, pp. 324-328 (2007)

学会発表

- 日本航空宇宙学会 第 38 期年会講演会、東京、2007 年、4 月
「イントラキャビティ吸収分光法による高エンタルピー気流診断法の開発」
- 宇宙航行の力学シンポジウム、神奈川、2007 年、12 月
「Cr:LiSAF レーザーを用いた高エンタルピー流診断のための高感度吸収分光法の開発」
- The 6th Asia Pacific Laser Symposium, Nagoya, 2008 年、2 月
「Development of Intra Cavity Absorption Spectroscopy System Using Cr:LiSAF CW Laser For Plasma Diagnostics」